# Cumulonimbus Clouds Convert a Smaller Fraction of CAPE into Kinetic Energy in a Warmer Atmosphere

JOHN M. PETERS, a DANIEL R. CHAVAS, ZACHARY J. LEBO, AND CHUN-YIAN SU

Department of Meteorology and Atmospheric Science, The Pennsylvania State University, University Park, Pennsylvania
 Department of Earth, Atmospheric, and Planetary Sciences, Purdue University, West Lafayette, Indiana
 School of Meteorology, University of Oklahoma, Norman, Oklahoma

(Manuscript received 12 January 2024, in final form 13 August 2024, accepted 3 September 2024)

ABSTRACT: This study investigates how entrainment's diluting effect on cumulonimbus updraft buoyancy is affected by the temperature of the troposphere, which is expected to increase by the end of the century. A parcel model framework is constructed that allows for independent variations in the temperature (T), the entrainment rate  $\varepsilon$ , the free-tropospheric relative humidity (RH), and the convective available potential energy (CAPE). Using this framework, dilution of buoyancy is evaluated with T and RH independently varied and with CAPE either held constant or increased with temperature. When CAPE is held constant, buoyancy decreases as T increases, with parcels in warmer environments realizing substantially smaller fractions of their CAPE as kinetic energy (KE). This occurs because the increased moisture difference between an updraft and its surroundings at warmer temperatures drives greater updraft dilution. Similar results are found in midlatitude and tropical conditions when CAPE is increased with temperature. With the expected 6%–7% increase in CAPE per kelvin of warming, KE only increases at 2%-4% K<sup>-1</sup> in narrow updrafts but tracks more closely with CAPE at 4%-6% in wider updrafts. Interestingly, the rate of increase in the KE with T becomes larger than that of CAPE when the later quantity increases at more than 10% K<sup>-1</sup>. These findings emphasize the importance of considering entrainment in studies of moist convection's response to climate change, as the entrainment-driven dilution of buoyancy may partially counteract the influence of increases in CAPE on updraft intensity.

SIGNIFICANCE STATEMENT: Cumulonimbus clouds mix air with their surrounding environment through a process called entrainment, which controls how efficiently environmental energy is converted into upward speed in thunderstorm updrafts. Our research shows that warmer temperatures will exacerbate the moisture difference between cumulonimbus updrafts and their surroundings, leading to greater mixing and less efficient conversion of environmental energy into updraft speeds. This effect should be considered in future research that investigates how climate change will affect cumulonimbus clouds.

KEYWORDS: Deep convection; Entrainment; Thunderstorms; CAPE; Climate change; Thermodynamics

#### 1. Introduction

The entrainment of dry air from the free troposphere into cumulonimbus updrafts dilutes the clouds' core buoyancy and substantially influences the vertical velocity and vertical mass flux (e.g., Zhang et al. 2003; Romps and Kuang 2010b; Singh and O'Gorman 2013a, 2015; Peters et al. 2019, 2020b, 2023a). Entrainment-driven dilution (hereafter simply "dilution") is an essential element to cumulus parameterizations (e.g., Arakawa and Schubert 1974), and a lack of consensus for how entrainment should be formulated in cumulus parameterizations contributes to substantial uncertainty in predictions by global climate models (GCMs; e.g., Donner et al. 2016; Christopoulos and Schneider 2021). Improving our fundamental understanding of entrainment in cumulus clouds is therefore critical to understanding and predicting our global climate system.

Given that the planet is warming and that temperatures on convective days will become warmer in plausible future climate scenarios (e.g., Lepore et al. 2021), it is important to understand how dilution is affected by temperature. To provide

Corresponding author: John M. Peters, john.m.peters@psu.edu

context for why such a dependency on temperature might exist, we consider the classical entraining plume equation for the moist static energy h of a parcel rising through a cloudy updraft (which describes the dilution of h):

$$\frac{dh}{dz} = -\varepsilon(h - h_0),\tag{1}$$

where  $\varepsilon$  is the fractional entrainment rate and we have assumed h is adiabatically conserved. Other variable definitions in this and subsequent equations are available in the table in appendix A.

The "deficit" in h between a parcel and its surrounding environment,  $h - h_0$ , is given by

$$h - h_0 = c_{nd}(T - T_0) + L_{\nu}(q^* - RH_0 q_0^*).$$
 (2)

To simplify our interpretation of this equation, we assume that  $q^* \approx q_0^*$ , which is reasonable given the typically modest temperature excesses (and, by extension, saturation excesses) of updrafts relative to their surroundings (e.g., Romps and Oktem 2015). We then combine Eq. (2) with Eq. (1) and use the result to write the contribution to the dilution of h with

height from the second term on the right-hand side (rhs) of Eq. (2) (denoted with the subscript m) as follows:

$$\frac{\partial h}{\partial z_m} = -\frac{R_v L_v}{R_d p_0} \varepsilon (1 - RH_0) e_0^*, \tag{3}$$

where the saturation vapor pressure  $e_0^*$  of the environment is given as a function of temperature by the Clausius–Clapeyron relation. This equation specifically pertains to a parcel's period of ascent in the free troposphere once it achieves saturation.

From Eq. (3), it is clear that an updraft will experience the greatest dilution when its entrainment rate is large (i.e., large  $\varepsilon$ ) and the environment is the driest [i.e., small freetropospheric relative humidity (RH<sub>0</sub>)]. These dependencies are intuitive and are frequent topics in past scientific literature (see Romps 2010; Hannah 2017; Holloway and Neelin 2009; Morrison et al. 2020; Peters et al. 2020a, 2022a,b; Morrison et al. 2022). Less frequently discussed in past literature is the role of the  $e_0^*$  term, which increases exponentially with  $T_0$ , implying that entrainment drives more dilution at warmer temperatures, all else being equal. Conceptually, at a given freetropospheric RH<sub>0</sub>, the latent energy difference between a parcel and its environment increases with warming-it is this energy deficit that drives dilution based on Eq. (1). Obviously, Eq. (3) is a dramatic simplification of the real atmosphere and is merely used here to motivate hypotheses that will be addressed with more rigorous calculations later on in this article. For instance, we have neglected the first term on the right-hand side of Eq. (2), along with the temperature dependencies of heat capacities, latent heats, freezing and deposition, and adiabatic sources and sinks of h (e.g., Romps 2015). Our interpretation of Eq. (2) is also (potentially) invalidated if  $\varepsilon$  and/or RH<sub>0</sub> in the free troposphere change substantially with temperature. While we have little understanding of how  $\varepsilon$  depends on temperature, there is reason to believe that RH<sub>0</sub> in the free troposphere will only minimally change as the planet warms (O'Gorman and Muller 2010; Douville et al. 2022). Hence, the increase in dilution with temperature at a given freetropospheric RH<sub>0</sub> implied by Eq. (3) is a potentially important influence on how deep moist convection will respond to climate change.

Indeed, Trapp and Hoogewind (2016) observed that severe thunderstorm updrafts simulated in future warming scenarios were not appreciably more intense than their present climate counterparts despite larger CAPE in future environments. To explain this result, they hypothesized that entrainment dilutes updraft buoyancy to a greater extent at warmer temperatures. Similarly, Singh and O'Gorman (2015) showed that updraft kinetic energy (KE) increases at a far slower rate than CAPE with increasing sea surface temperatures in simulations of radiative-convective equilibrium (RCE), implying that storms become less efficient at converting CAPE into KE at warmer temperatures because of increasingly detrimental entrainment. Both of these results support our cursory examination of Eq. (3); however, they pertain to very specific atmospheric conditions, such as a few realizations of midlatitude storm environments in the case of Trapp and Hoogewind (2016) and RCE in the case of Singh and O'Gorman (2013b). Both of these studies also relied on simulations with kilometer-scale horizontal grid spacing, which is known to be inadequately fine for the explicit resolution of the flow structures responsible for entrainment (Varble et al. 2014; Morrison et al. 2020; Peters et al. 2020a). It is therefore difficult to generalize these results without a more comprehensive analysis, which motivates this paper.

Our objective is to quantify this temperature sensitivity of dilution across a range of atmospheric conditions. We do so while relaxing some of the assumptions that we invoked when discussing Eq. (3) and with a more complete set of physics that includes temperature dependencies of heat capacities and latent heat, freezing, and a more accurate budget equation for *h*. We specifically address the following hypotheses:

- H1: At fixed CAPE, updrafts will generally convert less CAPE into KE at warmer temperatures than they do at cooler temperatures.
- H2: Under plausible future changes in CAPE and RH<sub>0</sub>, updrafts will generally convert a smaller faction of CAPE into KE. Hence, the rate of increase in KE with warming is slower than the rate of increase in CAPE.

We should note that our understanding of how  $\varepsilon$  might change with warming is extremely limited, and we therefore make the (potentially invalid) status quo assumption that  $\varepsilon$  remains constant for the purposes of improving fundamental understanding. We will address potential changes to  $\varepsilon$  in future work.

We evaluate the aforementioned hypotheses by generating idealized atmospheric profiles with systematically varied temperature, RH<sub>0</sub>, CAPE, and undiluted buoyancy. We use an entraining parcel model to calculate the properties of air parcels lifted in these profiles to quantify dilution. Though our results are not specific predictions of changes, they lay a foundational understanding that will guide the interpretation of entrainment effects in GCM and cloud-resolving model (CRM) climate studies.

# 2. Parcel model analysis

#### a. Overview

Our analysis consists of a series of four parcel model experiments which quantify the dependency of dilution on temperature. Despite the comparative complexity of real-world updrafts, numerous previous studies have demonstrated that the fundamental dependencies of dilution on an updraft's environmental characteristics are accurately represented by parcel models (e.g., Romps and Kuang 2010a; Morrison 2016, 2017; Morrison et al. 2020; Peters et al. 2020b, 2022a,c, 2023b). Parcel models also offer the advantage of a low computational cost, allowing for their application over a wide environmental parameter space in a way that would be computationally infeasible for large eddy simulations.

Our experiments are summarized as follows:

 Constant buoyancy: This experiment targets H1. It isolates the fundamental dependence of dilution on temperature

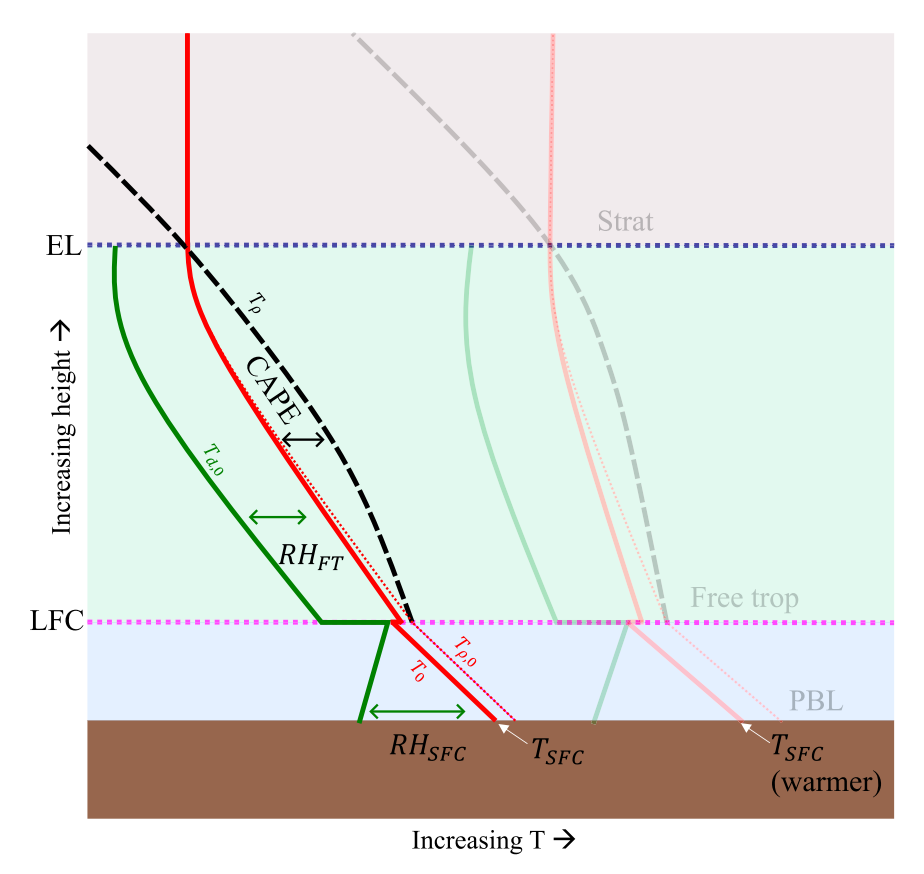


FIG. 1. Schematic illustrating the features of our procedure for generating environmental profiles. The three layers are delineated by shading, with blue shading denoting the PBL, green shading denoting the free troposphere, and red shading denoting the stratosphere. Environmental temperature  $T_0$ , density temperature  $T_{\rho,0}$ , and dewpoint temperature  $T_d$  are shown in solid red, red dashed, and green lines, respectively. The term  $T_\rho$  of an undiluted parcel is shown as a black dashed curve. Note that the slight increase in  $T_0$  at the bottom of the free troposphere ensures a smooth transition in  $T_{\rho,0}$  and undiluted buoyancy through this layer. An alternative profile with a warmer  $T_{\rm SFC}$  and all other attributes held constant is shown with translucent lines.

with other factors, such as  $RH_0$ , CAPE, the shape of the profile of undiluted buoyancy, and  $\varepsilon$ , held constant.

- Constant CAPE: This experiment also targets H1 by using observations from midlatitude cumulonimbus environments to form buoyancy profile shapes that evolve with temperature in a realistic manner.
- Increasing CAPE: This experiment targets H2. It uses observation-based buoyancy profiles and assigns CAPE an exponential dependence on temperature, which is an expectation of a warming climate.
- Coevolving CAPE, buoyancy, and RH: In our last experiment, we generate atmospheric profiles using an analytic model that encapsulates the coupled relationship between CAPE, buoyancy, temperature, and RH in the tropics. This experiment addresses H2.

#### b. Procedure for generating parcel environments

To accommodate our experiments, we devised a method for generating atmospheric profiles that can be systematically altered to satisfy prescribed conditions. For a visual aid, Fig. 1 shows a schematic illustrating the salient features of the profiles generated by this procedure (refer to Table A1 for variable definitions). Following Chavas and Dawson (2021), we divided the atmosphere into three distinct layers: a boundary layer with constant h (blue shading in Fig. 1), a free troposphere (green shading in Fig. 1) where temperature and moisture are determined by our profile generation procedure, and an isothermal stratosphere (red shading in Fig. 1). Independent predefined parameters are as follows:

- 1) Surface temperature ( $T_{\rm SFC}$ ), reflected by the horizontal position of the solid red line in Fig. 1.
- 2) Surface RH (RH<sub>SFC</sub>), represented by the difference between  $T_0$  and  $T_{d,0}$  at the surface (i.e., the dewpoint depression) in Fig. 1.
- 3) Profile of undiluted buoyancy  $(B_{\rm UD})$ , reflected by the separation between  $T_{\rho}$  (the black dashed curve) and  $T_{\rho,0}$  (the red dashed curve) at each height level in Fig. 1.

- 4) CAPE for an undiluted parcel, reflected by the total area between  $T_{\rho}$  and  $T_{\rho,0}$  in Fig. 1.
- 5) Free-tropospheric RH (RH<sub>FT</sub>), reflected by the separation between  $T_0$  (solid red) and  $T_{d,0}$  (solid green) in Fig. 1.
- 6) Equilibrium level (EL) height, reflected by the highest instance where  $T_{\rho} > T_{\rho,0}$  in Fig. 1.
- 7) Surface pressure  $p_{SFC}$ .

Using these input parameters, our procedure constructs profiles of environmental temperature  $T_0$ , water vapor mass fraction  $q_0$ , and pressure  $p_0$ . In this model, increasing the surface temperature while holding other factors constant will increase the temperature of the entire troposphere. This is evident in Fig. 1, where as  $T_{\rm SFC}$  warms, the entire profile warms too (rightward shift on the figure). This connection occurs because the temperature (and moisture) of the overlying atmosphere must accommodate the prespecified  $B_u$  and CAPE, and consequently, these variables are dependent on  $t_p$  of a lifted air parcel (which itself depends on  $t_p$ ). The remaining technical details of how  $t_p$ ,  $t_p$ , and  $t_p$ 0 were computed are available in appendix B.

#### c. Quantifying dilution

We quantify dilution by calculating the properties of entraining parcels ascended through these environments using lapse rate formulas for T and  $q_t$  from Peters et al. [2022c, Eqs. (24) and (36)–(38) therein], which yielded profiles of T,  $q_v$  (via a saturation assumption), and  $q_t$ . We then computed the buoyancy of the entraining parcel ( $B_E$ ) from the parcels' profiles of T,  $q_v$ , and  $q_t$ . These lapse rate formulas share the thermodynamic assumptions used to construct the environmental profiles in the previous subsection and represent mixing using a constant user-specified value of the fractional entrainment rate  $\varepsilon$ . Importantly, they are derived based on the Rankine–Kirchhoff approximations (Romps 2021) which account for the temperature dependence of latent heat and the moisture dependence of heat capacities, which are potentially important factors in how dilution responds to temperature.

Conceptually, wider updrafts are less diluted by entrainment than their narrower counterparts (e.g., Zhang et al. 2003; Morrison 2017). Thus, larger values of  $\varepsilon$  are representative of narrower updrafts, and smaller values of  $\varepsilon$  are representative of wider updrafts. In our calculations, we compute  $\varepsilon$  corresponding to the prescribed updraft R via the following formula from Eq. (4) in Morrison et al. (2020):

$$\varepsilon = \frac{2k^2 L_{\text{mix}}}{P_{\text{s}} R^2},\tag{4}$$

where  $k^2=0.18$  is the squared von Kármán constant,  $L_{\rm mix}=120$  m is a constant mixing length, and  $P_r=1/3$  is the turbulent Prandtl number [these parameter values are based on Morrison et al. (2021) and Peters et al. (2022b, 2023a)]. This formula was derived using an eddy diffusivity approximation for the lateral mixing between an updraft and its surroundings. Importantly, the parcel model assumes that  $\varepsilon$  remains constant with height. Previous studies that calculate both direct entrainment rates and bulk entrainment rates support the

idea that  $\varepsilon$  is approximately steady with height in individual updrafts (e.g., Romps 2010; Peters et al. 2020c; Lasher-Trapp et al. 2021). Our analysis primarily investigates two updraft radii. For narrow updrafts, we set R=1000 m yielding  $\varepsilon=0.13$  km, which is on par with bulk fractional entrainment rates diagnosed from tropical deep convection (e.g., Fig. 8 in Romps 2010), from weakly sheared midlatitude deep convection (Fig. 12a in Peters et al. 2020c), and during the incipient stages of organized continental deep convection (e.g., Fig. 6c in Lasher-Trapp et al. 2021). A second value of R=2000 m yields  $\varepsilon=0.032$  km and represents wider updrafts characteristic of organized deep convection [see  $\varepsilon$  during the mature phase of supercells shown in Fig. 6c of Lasher-Trapp et al. (2021)].

With  $\varepsilon$  for 1000- and 2000-m R updrafts at hand, we integrated the parcel model upward with a forward Euler scheme and a vertical grid spacing of 2.5 m. We set the precipitation rate in the Peters et al. (2022c) lapse rate formulas ( $\mathbb P$  in those studies) to 0, which is tantamount to assuming that the only condensate sink occurs via entrainment (those authors found the behavior of total water along the updraft core trajectories in simulations to be most consistent with the  $\mathbb P=0$  assumption).

We quantify dilution by assessing the percentage of CAPE that an entraining parcel realizes using the following formula:

$$\tilde{E} = 100 \times \frac{\text{KE}}{\text{CAPE}},\tag{5}$$

where  $\mathrm{KE} = \int_{\mathrm{LFC}}^{\mathrm{EL}} B_E dz$  is the buoyant kinetic energy realized by the diluted updraft parcel; LFC is the level of free convection, defined as the height of the first instance of positive buoyancy along the parcel's path of ascent; and EL is the equilibrium level, defined as the height of the last instance of positive buoyancy. The parameter  $\tilde{E}$  ranges from 0% (no CAPE realized as KE; strong dilution) to 100% (all CAPE realized as KE; no dilution). Both hypotheses H1 and H2 from the introduction imply a decrease in  $\tilde{E}$  with temperature—in other words,  $\partial \tilde{E}/\partial T_{\mathrm{SFC}} < 0$ .

#### d. Constant buoyancy experiment

The most effective way to isolate the fundamental dependence of  $\tilde{E}$  on temperature at a given value of CAPE (i.e., to address H1) is to vary temperature while holding as many other parameters as possible constant. This includes holding the shape of the profile of undiluted buoyancy  $B_{\rm UD}$  fixed as temperature changes. As will be shown shortly, the profile of  $B_{\rm UD}$  will typically change shape as temperature changes in nature, and we will account for this connection in our second experiment.

 $<sup>^1</sup>$  The latter two studies use direct measures of entrainment and show  $\varepsilon$  that is roughly double the  $\varepsilon=0.13$ -km value used here. However, the values used in our study are most comparable to bulk entrainment rates, which are typically about half of their directly measured counterparts (Romps 2010). Hence, our number corresponds well with theirs.

We use a simple two-mode sinusoidal function to prescribe  $B_{\rm UD}$  with the following formula:

$$B_{u}(z) = \frac{\text{CAPE}}{\pi(z_{\text{EL}} - z_{\text{BL}})} \left[ \sin \left( \pi \frac{z - z_{\text{BL}}}{z_{\text{EL}} - z_{\text{BL}}} \right) - \sin \left( 2\pi \frac{z - z_{\text{BL}}}{z_{\text{EL}} - z_{\text{BL}}} \right) \right]. \tag{6}$$

This analytic function is designed to produce a smooth profile of  $B_{\rm UD}$  with maximum values in the upper troposphere, consistent with typical conditions in the real atmosphere (see, e.g., Fig. 2 in Singh and O'Gorman 2013b). Profiles of skew T diagrams at two different  $T_{\rm SFC}$  values generated for this experiment are shown in Fig. 2a, and the undiluted buoyancy profiles corresponding to five different  $T_{\rm SFC}$  values are shown in Fig. 2b (they all overlap because they share the same buoyancy profile). Note that despite the  $B_{\rm UD}$  profiles overlapping, diluted buoyancy profiles show noticeable differences from one another foreshadowing later results.

#### e. Constant CAPE experiment

In reality, the shape of the profile of  $B_{\rm UD}$  typically covaries with  $T_{SFC}$  at a given value of CAPE. If H1 is relevant to cumulonimbus clouds in nature, this hypothesis should remain valid under these covariations of  $B_{\rm UD}$  and  $T_{\rm SFC}$ . Our second experiment therefore uses a procedure for generating profiles that allows  $B_{\rm UD}$  to vary with  $T_{\rm SFC}$  in a manner consistent with observed soundings. We accomplished this using the proximity sounding database of Thompson et al. (2003) (hereafter T03), which contains 1098 Rapid Update Cycle and Rapid Refresh derived profiles taken near observed severe hail, straight-line wind, and tornado events in the contiguous United States. From these soundings, we generated a total of four composite profiles of  $B_u$  with all soundings whose CAPE fell within ±300 J kg<sup>-1</sup> of 2000 and 3000 J kg<sup>-1</sup> and whose  $T_{\rm SFC}$  fell within  $\pm 1$  K of 295 and 305 K. When the procedure is used to generate a sounding with  $T_{SFC}$  and/or CAPE that differ from the values in these composites, a profile of  $B_{\rm UD}$ was generated via bilinear interpolation (or extrapolation) at each height from the values of  $T_{SFC}$  and CAPE in the composites onto the user-specified values. We then input this composite-sounding generated  $B_u$  (and the corresponding EL height) into our profile generation procedure to generate corresponding profiles of  $T_0$ ,  $q_0$ , and  $p_0$ . This strategy ensures a smooth transition in profile characteristics across values of  $T_{\rm SFC}$ . Comparison of the  $T_{\rm SFC}$  = 295 and 305 K profiles at 2000 J kg<sup>-1</sup> reveals a 2-4-km upward shift in both the height of maximum  $B_{\rm UD}$  and the EL in the warm profiles relative to the cool ones (Figs. 2c,d), along with slightly smaller  $B_{\rm UD}$  below 1 km in the warm profiles than in the cool profiles. The mean RH<sub>SFC</sub> among all T03 soundings was roughly 65%. Hence, we set  $RH_{SFC} = 65\%$  in both this and the constant buoyancy experiment.

### f. Increasing CAPE experiment

As was discussed earlier, CAPE is expected to increase as the planet warms. This motivated an additional experiment to validate H2, wherein we allowed CAPE to vary with  $T_{\rm SFC}$  as

is expected in the real world. In the tropics, theory suggests that CAPE should increase exponentially at roughly 6%-7% K<sup>-1</sup> (Romps 2016). This trend closely follows the temperature dependency of the saturation mixing ratio, which increases at roughly 7% K<sup>-1</sup> at 300 K based on the Clausius-Clapeyron relation. There is some theoretical evidence that the increase in CAPE should be exponential in the midlatitudes as well (e.g., Agard and Emanuel 2017). However, the precise rate of increase is somewhat uncertain. For instance, Diffenbaugh et al. (2013) (their Fig. 3) and Trapp and Hoogewind (2016) (their Fig. 1) show roughly 6-7 K of temperature increase in the continental United States over the next century under the RCP8.5 emissions scenario based on analyses of climate models from phase 5 of the Coupled Model Intercomparison Project (CMIP5). Trapp and Hoogewind (2016) simulated three historic severe thunderstorm events with the pseudo-global warming technique and found CAPE increases of roughly 5%, 14%, and 4% K<sup>-1</sup> among these cases. Based on their results, we select a value of 6% for the example profiles shown in Figs. 2e and 2f and the detailed analysis in section 3b. We also set  $RH_{SFC} = 65\%$  in this experiment though we also perform a sensitivity test to RH<sub>SFC</sub> that is detailed later on.

We use the observation-based procedure for determining buoyancy profiles from the previous experiment to construct  $B_u$  profiles for this experiment. We also increase CAPE with temperature using the formula:

$$CAPE(T_{SFC}) = CAPE_{290}e^{r(T-290)},$$
 (7)

where CAPE<sub>290</sub> is a reference value valid at 290 K and r is the rate of fractional increase with temperature (i.e., the percentage increase per kelvin divided by 100%). Example skew T diagrams (Fig. 2e) and undiluted buoyancy profiles (Fig. 2f) show how profiles generated by the T03 procedure respond to increasing CAPE 6% K<sup>-1</sup>. These plots reveal that as  $T_{\rm SFC}$  and CAPE increase, buoyancy primarily increases aloft and the tropopause height rises sharply (Figs. 2e,f). This dependency of buoyancy profiles on  $T_{\rm SFC}$  closely mimics the behavior of the analytic profiles projecting future changes in the tropics (Romps 2016; e.g., Fig. 7 therein).

# g. Exploring a range of rates of increase in CAPE with warming

Because of the uncertainty in the percentage increase in CAPE per kelvin expected with warming in the midlatitudes, we also evaluate CAPE increase from 0% to 15% K $^{-1}$  on dilution. To create a distribution of parameters that characterize typical severe weather environments, we used the values of CAPE,  $T_{\rm SFC}$ , and RH $_{\rm FT}$  (averaged within the 2–7-km layer) from the T03 sounding (three quantities per sounding) to generate a set of 1098 profiles that represent our present climate. We then increase  $T_{\rm SFC}$  in each of these profiles by 5 K and increase CAPE ranging from 0% to 15% K $^{-1}$  over this 5-K temperature increase using Eq. (7). Finally, we evaluate the range of relative changes in KE (expressed as a percentage per kelvin) with increasing  $T_{\rm SFC}$  as a function of the specified relative increase in CAPE with warming (also expressed

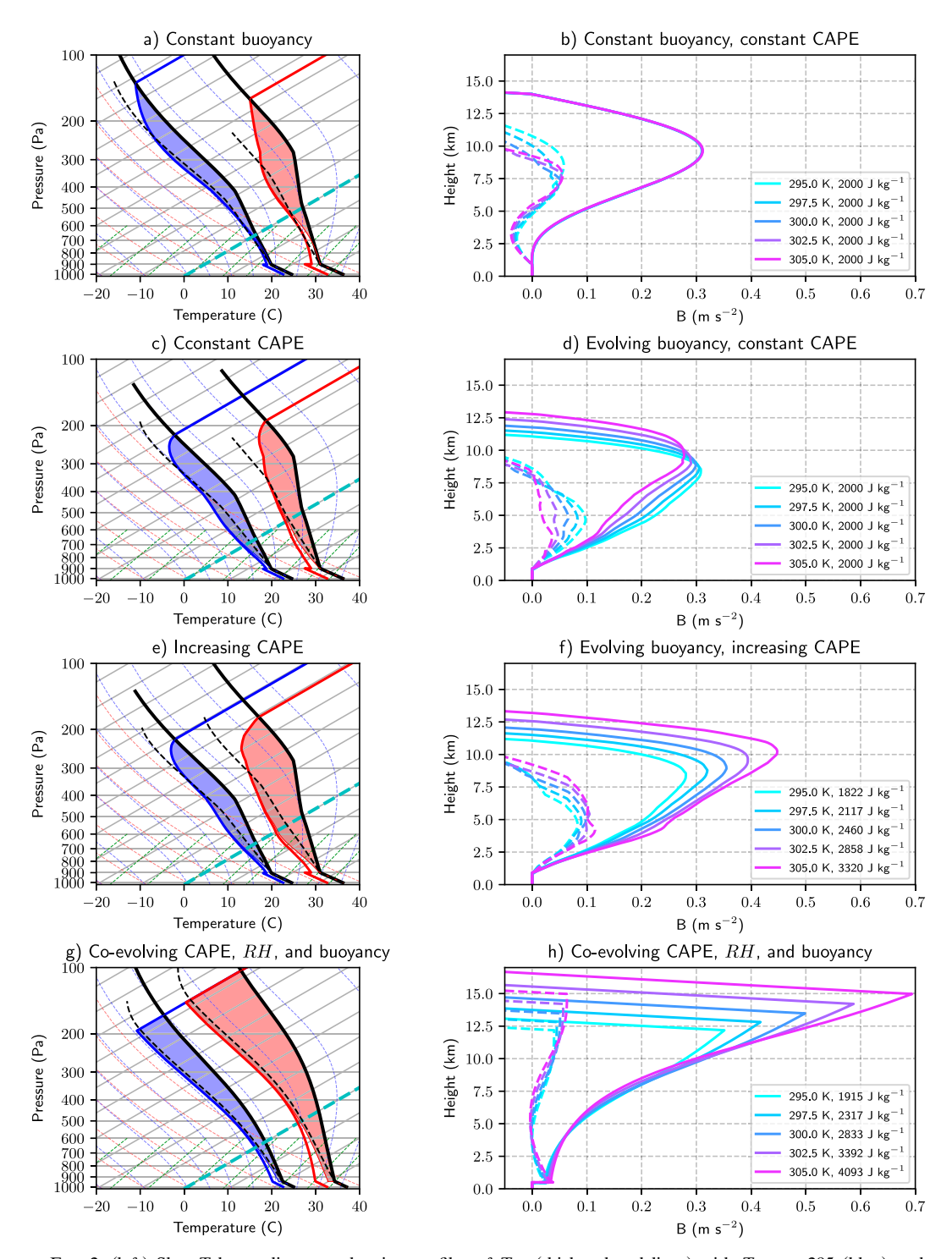


FIG. 2. (left) SkewT-log p diagrams showing profiles of  $T_{\rho,0}$  (thick colored lines) with  $T_{\rm SFC}=295$  (blue) and  $T_{\rm SFC}=305$  K (red),  $T_{\rho}$  of an undiluted lifted air parcel (thick black lines), and  $T_{\rho}$  of diluted lifted air parcels with R=1000 m (black dashed lines). Shading corresponds to CAPE. (right) Profiles of  $B_u$  (solid; m s<sup>-1</sup>) and  $B_E$  (dashed; R=1000 m) corresponding to the  $T_{\rm SFC}$  and CAPE values listed in the legend, with CAPE increasing with  $T_{\rm SFC}$  at a rate of 6% K<sup>-1</sup>. (a),(b) Constant buoyancy experiment. (c),(d) Constant CAPE experiment. (e),(f) Increasing CAPE experiment. (g),(h) Coevolving CAPE, RH, and buoyancy experiment.

as a percentage per kelvin). This analysis tells us whether the rate of increase of KE with  $T_{\rm SFC}$  underpaces, matches, or outpaces the analogous increase in CAPE, implying decreasing, constant, and increasing  $\tilde{E}$  with  $T_{\rm SFC}$ , respectively. This last analysis also analyzes updraft radii of 750 m, in addition to 1000- and 2000-m values used in prior experiments.

# h. Coevolving CAPE, buoyancy, and RH experiment

In the tropics, there is a coupled relationship between temperature, free tropospheric RH, and CAPE. This occurs because of a feedback between convection and its environment, whereby detrained water and compensating subsidence adjust the atmosphere, altering the CAPE and consequently altering the intensity of convection. A series of articles including Singh and O'Gorman (2013b) and Romps (2014, 2016) have developed theoretical frameworks to account for this coupled relationship, which is used to project the coupled relationship between free-tropospheric RH, CAPE, and temperature across a range of atmospheric temperatures. Our final experiment calculates  $T_0$  and  $q_0$  above the lifted condensation level (LCL) using the analytic model introduced by Romps (2014) (detailed in appendix C) and with the same  $T_{\rm SFC}$  range used in previous experiments.

The most important free parameter in this model is the mean fractional entrainment rate  $\varepsilon_m$  experienced across the population of convective clouds in the tropics. The model calculates profiles of temperature and moisture under the assumption that these profiles have equilibrated to the compensating subsidence and detrainment driven by the mean cloud population. We select a value of  $\varepsilon_m = 2.5 \times 10^{-4} \,\mathrm{m}^{-1}$ , which is intentionally larger than  $\varepsilon$  values of  $\varepsilon_m = 1.3 \times 10^{-4}$  and  $0.32 \times 10^{-4}$  m<sup>-1</sup> used to calculate  $\tilde{E}$ . This choice implicitly assumes that our calculated  $\tilde{E}$  values represent updrafts whose buoyancy is larger (and  $\varepsilon$  smaller) than that of the average cloud within a given convective environment. Another important free parameter in this model is  $\beta$  (see appendix C), which controls the amount of condensate that evaporates into the cloud's environment (increased by raising  $\beta$ ) or leaves the atmosphere as rain (increased by decreasing  $\beta$ ). To represent uncertainty in this parameter, we evaluate the model with  $\beta$  ranging from 0 to 0.9. Finally, we set the RH<sub>SFC</sub> to 80% in this experiment to reflect the values that typify the tropics (e.g., Fig. B2 in Chen et al. 2020).

## 3. Results

# a. Temperature dependency of $\tilde{E}$ at constant CAPE

Results from the constant CAPE (2000 J kg $^{-1}$ ) and constant buoyancy experiment are shown in Figs. 3a–d for R=1000- and 2000-m updrafts, respectively, with  $\tilde{E}$  and  $\partial \tilde{E}/\partial T_{\rm SFC}$  expressed as a function of  $T_{\rm SFC}$  and RH<sub>FT</sub>. For  $T_{\rm SFC} < 305$  K,  $\tilde{E}$  generally decreases as  $T_{\rm SFC}$  increases, which is reflected by a slant in the  $\tilde{E}$  contours toward the upper right in Figs. 3a and 3c and prevalent green shading in Figs. 3b and 3d (indicating negative  $\partial \tilde{E}/\partial T_{\rm SFC}$ ). In other words, at a given CAPE, RH<sub>FT</sub>, and  $\varepsilon$ , updrafts will experience more dilution at warmer temperatures, consistent with H1. This behavior is visually evident in Fig. 2b, wherein

 $B_u$  remains fixed across the range of  $T_{\rm SFC}$  investigated, whereas  $B_E$  decreases (particularly aloft) as  $T_{\rm SFC}$  increases. Dilution completely extincts the buoyancy of narrow updrafts in a dry atmosphere at sufficiently warm temperatures (white shading in the lower right of Fig. 3a), whereas narrow updrafts in a comparably dry but cool atmosphere realize up to 25% of their CAPE as KE (pink shading in the lower left of Fig. 3a). Results are qualitatively identical for other values of CAPE (not shown).

More generally,  $\tilde{E}$  is more sensitive to  $T_{\rm SFC}$  when the free troposphere is dry than when it is moist, as is indicated by darker greens on the lower-left side of Figs. 3b and 3d. Narrower updrafts also experience a greater temperature sensitivity than their wider counterparts, as indicated by darker greens in Fig. 3b for the R=1000-m updrafts than in Fig. 3d for the R=2000-m updrafts. Interestingly, the aforementioned trends reverse when  $T_{\rm SFC}>305$  K, and  $\tilde{E}$  actually increases with  $T_{\rm SFC}$ . This trend reversal coincides with the increasing contribution to  $B_u$  from condensates and water vapor effects at warmer temperatures. This is likely an artifact of  $B_u$  being (unrealistically) held constant across a wide range of temperatures, as will become clear when we allow the buoyancy to vary with  $T_{\rm SFC}$  in a realistic manner in the next experiment.

We have established that H1 is supported (for  $T_{SFC} < 305 \text{ K}$ ) when the buoyancy profile is held constant. What about when we evolve the buoyancy profile with temperature in a manner consistent with observations? Figs. 3e-h are directly analogous to Figs. 3a-d but show results from the constant CAPE experiment (again with CAPE set to 2000 J kg<sup>-1</sup>). The results of this second experiment are qualitatively similar, except that  $\partial \tilde{E}/\partial T_{SEC}$  is now negative for temperatures up to (and perhaps beyond) 310 K (Figs. 3f,h). Once again, we can see this in the buoyancy profiles in Fig. 2d. While  $B_u$  changes shape but maintains a roughly consistent magnitude as  $T_{\rm SFC}$ changes,  $B_E$  decreases considerably in magnitude as  $T_{SFC}$  increases. At warm temperatures, dilution nearly entirely extincts buoyancy of narrow updrafts for RH<sub>FT</sub> up to 50% (white shading in lower right of Fig. 3e), whereas narrow updrafts with comparable RH<sub>FT</sub> in cool environments convert 25%-40% of their CAPE into KE (pink shading in lower left of Fig. 3e). In other words, this experiment also supports H1, in that less CAPE is converted into KE at warmer temperatures than it is at cooler temperatures (all else being equal). Again,  $\tilde{E}$  is more sensitive to  $T_{\rm SFC}$  when the atmosphere is dry (greens are darkest in the lower part of Figs. 3f,h) and when updrafts are narrow (greens at a given location are darker in Fig. 3f than they are in Fig. 3h). An exception to this statement is for the warmest and driest environments (the lower-right corner of figures), where dilution completely extincts updraft buoyancy in the narrowest updrafts (Fig. 3e) and  $\partial \tilde{E}/\partial T_{\rm SFC}$  consequently ceases to be meaningful. The physical processes responsible for why  $\tilde{E}$  decreases with increasing  $T_{SFC}$  become clear when we break down our analysis of  $\tilde{E}$  into the individual contributions from the different terms contributing to buoyancy. Following Peters et al. (2023c), we may write an approximate equation for buoyancy as follows:

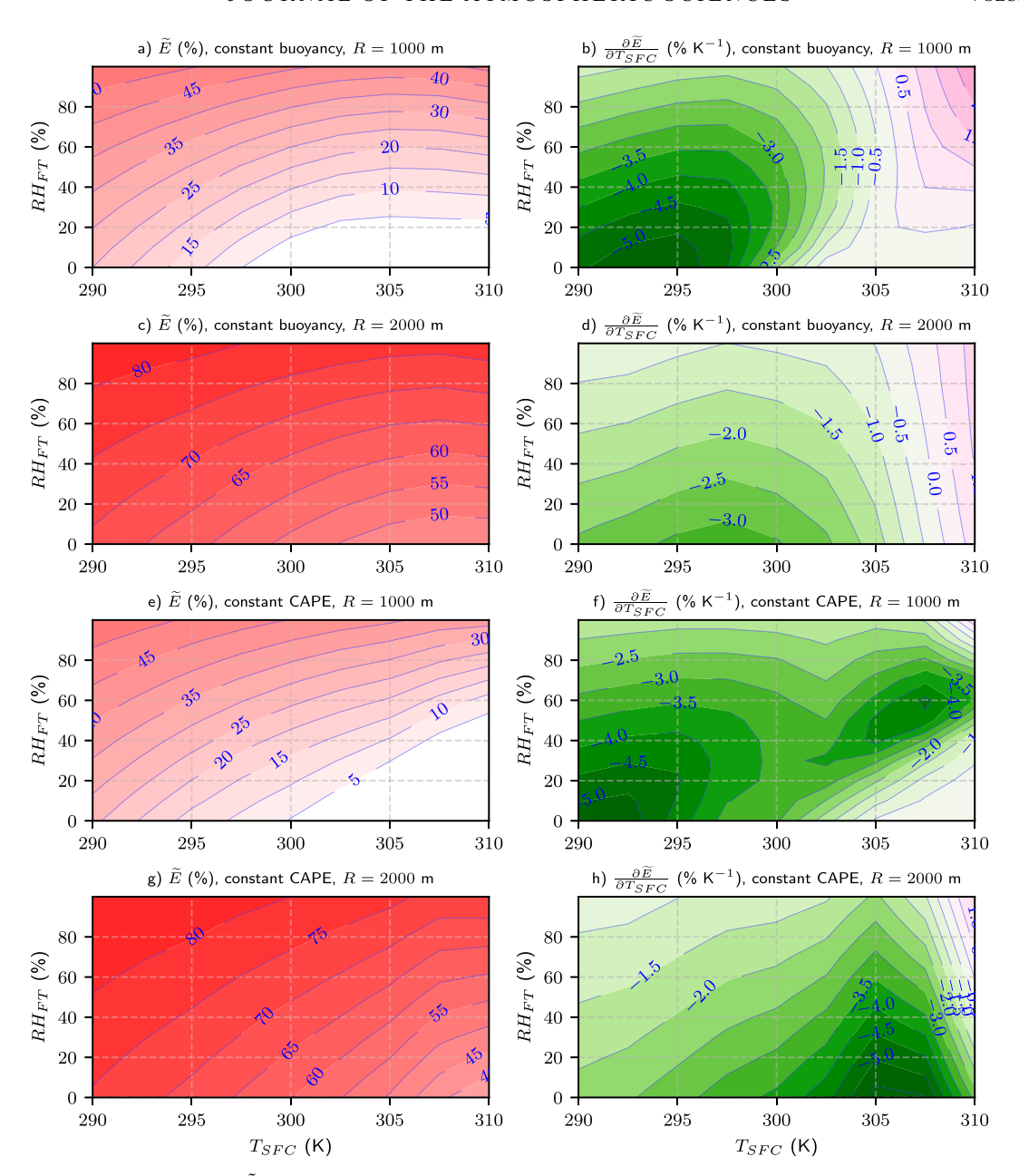


FIG. 3. (left) The term  $\tilde{E}$  (shading; %) as a function of  $T_{\rm SFC}$  (x axis; K) and RH<sub>FT</sub> (y axis; %). (right) The term  $\partial \tilde{E}/\partial T_{\rm SFC}$  (shading; % K<sup>-1</sup>) as a function of  $T_{\rm SFC}$  (x axis; K) and RH<sub>FT</sub> (y axis; %). (a),(b) Constant buoyancy, constant CAPE experiment with R=1000 m. (c),(d) Constant buoyancy, constant CAPE experiment with R=2000 m. (e),(f) Evolving buoyancy, constant CAPE experiment with R=2000 m.

$$B = g \frac{T_p - T_0}{T_0} + g \left(\frac{R_v}{R_d} - 1\right) (q_v - q_0) + g \frac{T - T_p}{T_0} - g(q_t - q_v),$$
(e) thermal condensate
(e) net condensate
(f) net water (6)

where  $T_p$  is the temperature of an entraining parcel whose condensates are immediately offloaded once they form (akin to a pseudoadiabatic parcel), calculated with Eq. (42) in Peters et al. (2022c); term (a) represents the thermal buoyancy that would occur in the presence of condensation and deposition if condensates were immediately removed; term (b) represents water vapor influences on parcel density and buoyancy; term (c) represents the net influence of condensates on the parcel's thermal buoyancy; term (d) represents condensate loading; and term (e) represents the net condensate influences on buoyancy. Term (c) includes physical effects, such as the latent heat released during the freezing of liquid, the slightly larger heat capacity of condensate-laden air, and the slight differences in pressure-volume work done by a condensate-laden parcel (see the supplemental file in Peters et al. 2023c). This term is usually positive because the latent heat and heat capacity effects increase the parcel temperature above the freezing level relative to what it would have been without condensate effects and freezing. Term (d), on the other hand, is always negative when condensate is present, and whether or not condensates contribute a net positive or negative influence on buoyancy depends on the sum of these two terms in term (e). Finally, term (f) represents all water effects. Terms (a) and (c) together represent a parcel's net thermal buoyancy [they sum to  $g(T - T_0)/T_0$ ].

In applying this buoyancy decomposition to the evolving buoyancy, constant CAPE experiments, we see that pseudothermal buoyancy contributions to  $\tilde{E}$  (Figs. 4c,d) show very similar magnitudes and distributions to that of the total  $\tilde{E}$ (Figs. 4a,b). Water vapor contributions are generally small for narrow updrafts (Fig. 4e) and over most of the wide updraft parameter space (Fig. 4f). This term only contributes more than 10% when updrafts are wide,  $T_{\rm SFC}$  is large, and the free troposphere is dry (i.e., the lower right of Fig. 4f). Thermal condensate effects are generally small in narrow updrafts (Fig. 4g) but become larger in wider updrafts at intermediary values of  $T_{SFC}$  (Fig. 4h). However, positive thermal condensate effects are more than offset by universally negative condensate loading, which is a bit larger in magnitude and is also maximized in magnitude for large T<sub>SFC</sub> and RH<sub>FT</sub> (Figs. 4i,j). Finally, the sum of vapor effects, thermal condensate effects, and condensate loading (net water effects, Figs. 4k,l) is generally small in magnitude at temperatures less than 300 K, indicating broad compensation between these terms over a range of conditions (Figs. 4k,l; similar to what was found by Grabowski and Morrison 2021). At larger temperatures, net water effects become increasingly important in narrow updrafts (Fig. 4k; less so in wide updrafts, Fig. 41), becoming negative at large RH<sub>ET</sub> and positive at small RHFT, though net buoyancy vanishes at large  $T_{\rm SFC}$  and small RH<sub>FT</sub> meaning that the later result is questionably physically meaningful. Hence, increasing  $T_{\rm SFC}$  primarily reduces  $\tilde{E}$  via a reduction in condensation and the associated impact on thermal buoyancy, along with an increasing negative contribution from condensate loading when  $T_{\rm SFC} > 305$  K.

#### b. Temperature dependency of $\tilde{E}$ with increasing CAPE

We now recast our analysis so that CAPE increases at  $6\% \text{ K}^{-1}$  of  $T_{SFC}$ , starting at  $1000 \text{ J kg}^{-1}$  at  $T_{SFC} = 290 \text{ K}$ . Recall

that the observed soundings used to determine buoyancy profiles were obtained near thunderstorm events in the midlatitude contiguous United States, making the results of these experiments most relevant to the midlatitudes. In this case,  $\tilde{E}$  still decreases with increasing  $T_{\rm SFC}$  consistent with H2, given that contours slant toward the upper right in Figs. 5a and 5c and green shading is prevalent in Figs. 5b and 5d. However, the rate of decrease of  $\tilde{E}$  with  $T_{SFC}$  (i.e.,  $\partial \tilde{E}/\partial T_{SFC}$ ) is substantially reduced relative to when CAPE was held constant, reflected by generally lighter green shading in Figs. 5b and 5d than in Figs. 3b, 3d, 3f, and 3h. This result implies that while  $\tilde{E}$  decreases with  $T_{\rm SFC}$  at a given CAPE,  $\tilde{E}$  increases with CAPE at a given  $T_{SFC}$ —a trend that will be discussed in more detail later on. It is also notable that in the case of increasing CAPE,  $\partial \tilde{E}/\partial T_{SFC}$  no longer shows a substantial dependency on RHFT (greens are more consistent in color throughout Figs. 5b,d than they are in Figs. 3b,d,f,h) or updraft radius (greens are similar in color in Figs. 5b,d). Hence, updrafts over a wide range of conditions will see similar 0.25%-0.75% decreases in  $\tilde{E}$  per kelvin.

Up to this point, we have analyzed how  $\tilde{E}$  changes with  $T_{\rm SFC}$  at a constant value of RH<sub>FT</sub>. Future projections of RH<sub>FT</sub> in the midlatitudes range from increases of a few percentages (e.g., Fig. 4b in Davis et al. 2023) to decreases of a few percentages (Fig. B2 in Chen et al. 2020). Given this uncertainty and the small magnitudes of projected changes, assuming a constant RHFT is reasonable. However, there is a comparative consensus that RH<sub>SFC</sub> will decrease with warming in the midlatitudes (e.g., Diffenbaugh et al. 2013; Trapp and Hoogewind 2016; Chen et al. 2020; Davis et al. 2023). How would this potential decrease affect our results? To address this question, we repeat the increasing CAPE experiment with the RH<sub>SFC</sub> linearly decreasing with temperature from 75% at  $T_{\rm SFC}$  = 290 K to 35% at  $T_{\rm SFC}$  = 310 K, which corresponds to a decrease of 2% K<sup>-1</sup> of warming and is roughly consistent with the findings in Davis et al. (2023).

Applying this adjustment reduces the magnitude of, and locally flips the sign of,  $\partial \tilde{E}/\partial T_{\rm SFC}$  at cold temperatures (i.e.,  $T_{\rm SFC} < 300$  K; compare Figs. 5f,h to Figs. 5b,d) but minimally alters  $\partial \tilde{E}/\partial T_{\rm SFC}$  at warmer temperatures. The reason for this is that decreasing RH<sub>SFC</sub> increases the PBL depth and lowers the temperature at which condensation occurs, effectively offsetting the warming environment at cold temperatures. At warmer temperatures, however, this effect is diminished due to the increasing rapidity at which moist adiabats steepen with temperature.

Do the physics responsible for the negative  $\partial \bar{E}/\partial T_{\rm SFC}$  change when CAPE increases with  $T_{\rm SFC}$ ? In examining the analogous contributions to buoyancy (Fig. 4) to those shown for the constant CAPE experiment in Fig. 6, we see that the trends in  $\tilde{E}$  (Figs. 6a,b) are nearly entirely explained by the trend in pseudo–thermal buoyancy (Figs. 6c,d), with minimal contribution from net water effects at all temperatures (Figs. 6e,f). This implies that the reduction in  $\tilde{E}$  with temperature as the climate warms is nearly entirely a consequence of a reduction in the thermal buoyancy achieved by ascending air parcels.

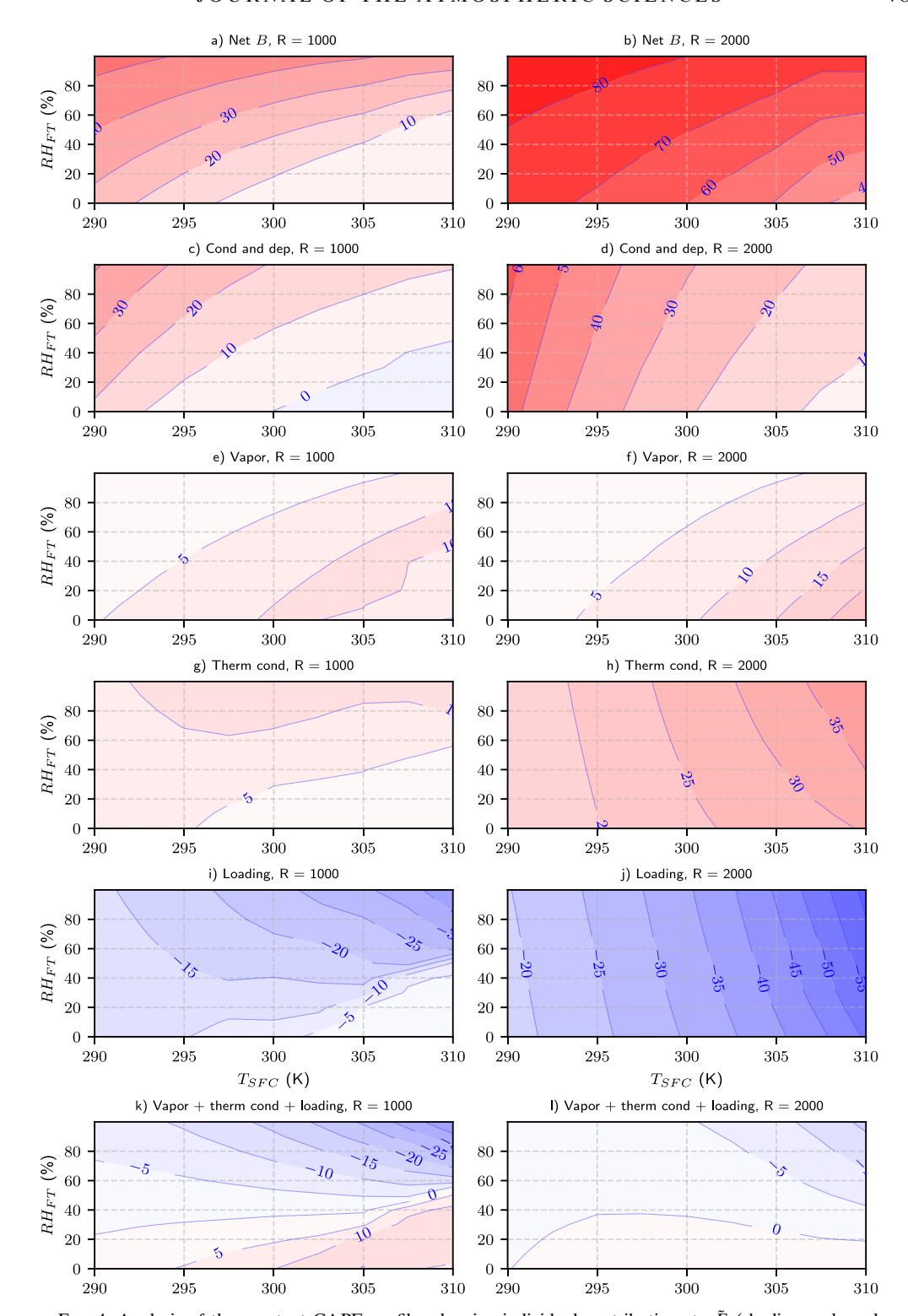


FIG. 4. Analysis of the constant CAPE profiles showing individual contributions to  $\tilde{E}$  (shading; reds and blues are positives and negatives, respectively). (first row) Contributions from all terms in Eq. (8) (this row is the same as Figs. 3e,f). (second row) Term (a) in Eq. (8), (third row) term (b) in Eq. (8), (fourth row) term (c) in Eq. (8), (fifth row) term (d) in Eq. (8), and (sixth row) the sum of terms (b), (c), and (d) in Eq. (8). (left)  $R = 1000 \, \text{m}$  and (right)  $R = 2000 \, \text{m}$ .

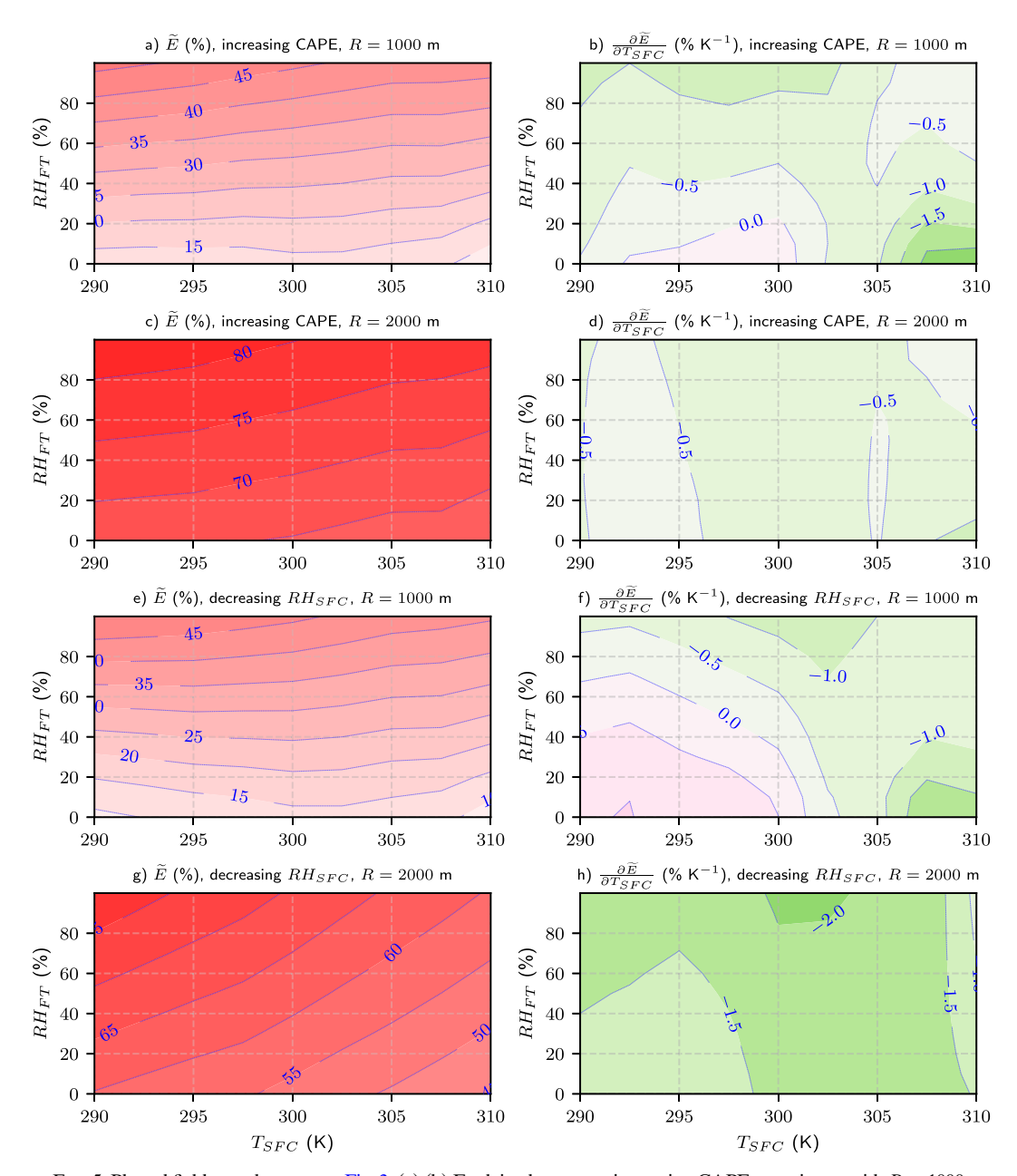


FIG. 5. Plotted fields are the same as Fig. 3. (a),(b) Evolving buoyancy, increasing CAPE experiment with R=1000 m. (c),(d) Constant buoyancy, evolving CAPE experiment with R=2000 m. (e)–(h) As in (a)–(d), but for RH<sub>SFC</sub> increased linearly from 35% at  $T_{\rm SFC}=290$  K to 75% at  $T_{\rm SFC}=310$  K.

#### c. Differences in the rates of increase of KE and CAPE

Relative changes in KE (i.e., % increases per kelvin) are also an important metric for assessing how updraft intensity will respond to warming. Here, we analyze the observation-based profiles described in section 2g to understand how the relative rate of increase in KE should compare to that of CAPE. We first consider the 6% K<sup>-1</sup> increase from the previous subsection's calculations and a 7% K<sup>-1</sup> increase characteristic of the Clausius–Clapeyron relation. In these scenarios,

there is a wide range of responses in KE for R=750-m updrafts ranging from -4% to 8% K<sup>-1</sup>, with a median near 2.5% K<sup>-1</sup>. Hence, in most cases, R=750-m updrafts will only minimally intensify with warming. Similarly, the rate of increase in KE for most R=1000-m updrafts is substantially slower than that of CAPE (Fig. 7a), with a range of 0%–6% K<sup>-1</sup> and a median of 3%–5% K<sup>-1</sup>. More generally, when CAPE increases by 10% K<sup>-1</sup> or less, rates of increase in KE substantially underpace rates of increase in CAPE for 750- and 1000-m-radius updrafts in most cases (Fig. 7a). This

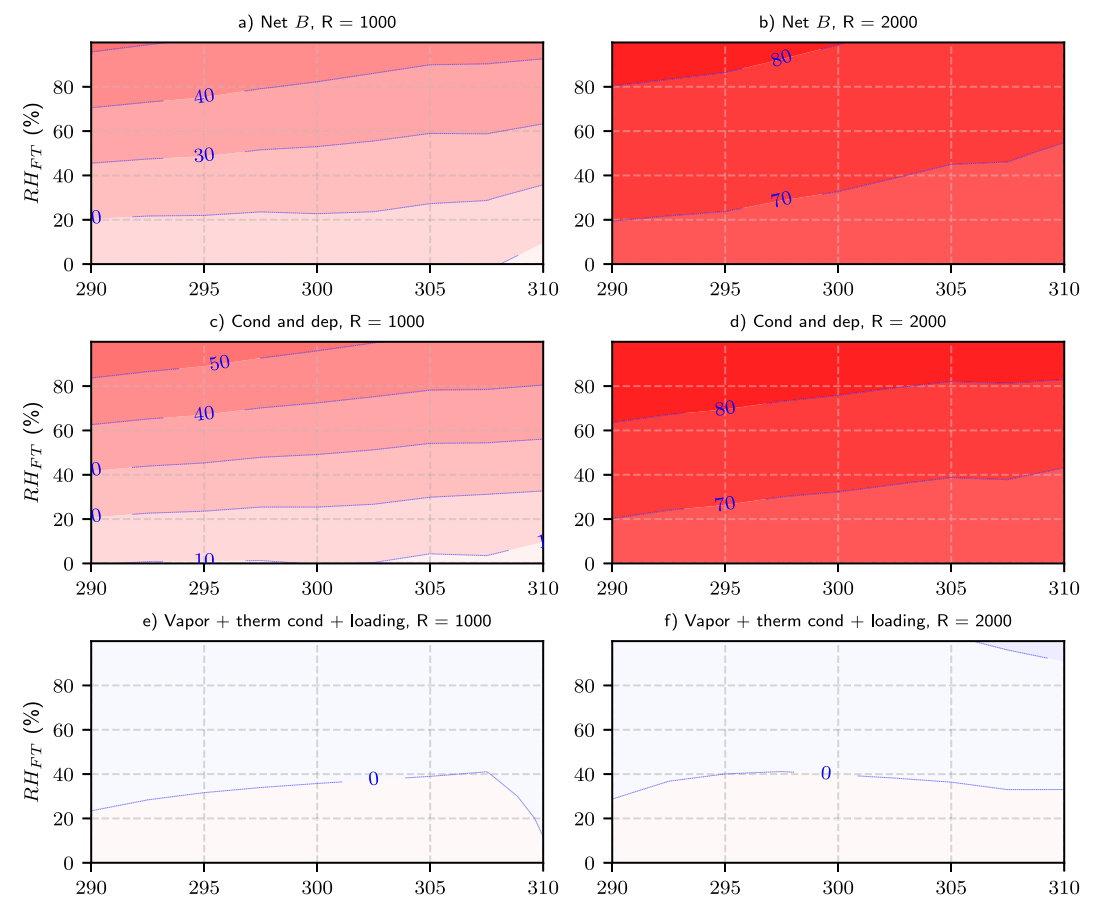


FIG. 6. As in Fig. 4, but for the increasing CAPE experiment.

behavior is visually evident in the  $B_U$  and  $B_E$  profiles shown in Fig. 2f. Notably, though  $B_E$  increases slightly with  $T_{\rm SFC}$ , this increase is much less pronounced than that of  $B_U$ , implying that less undiluted buoyancy is realized as entraining buoyancy at warmer temperatures. Hence, for physically reasonable rates of increase in CAPE with  $T_{\rm SFC}$ , narrow updrafts still generally realize less of their CAPE at warmer temperatures than they do at cooler temperatures. Relative increases in KE with temperature in 2000-m-radius updrafts are less sensitive to entrainment than in 1-km-radius updrafts, with the rate of change of KE with temperature tracking comparatively closer to that of CAPE.

Interestingly, for CAPE increases of 10%  $\rm K^{-1}$  or larger (i.e., well above the expected rate with warming), rates of increase of KE begin to outpace that of CAPE for all the R values considered here. This result is explained by the codependency of  $\tilde{E}$  on both  $T_{\rm SFC}$  and CAPE (Fig. 7b, shown for R=1000 m as an example). While  $\tilde{E}$  decreases with  $T_{\rm SFC}$  (as indicated by colors becoming lighter to the right in Fig. 7b),  $\tilde{E}$  increases with increasing CAPE (as indicated by colors becoming darker toward the top of Fig. 7b). When the increase in CAPE with  $T_{\rm SFC}$  is sufficiently small (e.g., 6%  $\rm K^{-1}$ ), curves of CAPE increase with  $T_{\rm SFC}$  (gray lines) generally move from darker colors to lighter colors in Fig. 7b reflecting that the tendency for  $\tilde{E}$  to decrease with  $T_{\rm SFC}$  "outpaces" the tendency for  $\tilde{E}$  to increase with CAPE. On the other hand, when the

increase in CAPE with  $T_{\rm SFC}$  is larger (e.g., 12% K $^{-1}$ ), curves of CAPE increase with  $T_{\rm SFC}$  (black lines) generally move from lighter colors to darker colors in Fig. 7b, reflecting that the tendency for  $\tilde{E}$  to increase with CAPE begins to outpace the tendency for  $\tilde{E}$  to decrease with  $T_{\rm SFC}$ .

# d. Temperature dependency of $\tilde{E}$ in the tropics with coevolving CAPE, buoyancy, and RH

It is reasonable to expect a variety of combinations of  $T_{\rm SFC}$ , RH $_{\rm FT}$ , and CAPE to occur in the midlatitudes where CAPE is determined by complicated factors such as differential advection (e.g., Markowski and Richardson 2010) and diurnal surface fluxes (e.g., Agard and Emanuel 2017). However, the atmospheric profiles of temperature and moisture in the tropics are largely determined by the vertical circulation driven by convection itself, leading to a much narrower range of possible parameter combinations in the tropics than in the midlatitudes. We encapsulate these interactions using the analytic model of Romps (2014) to generate profiles of  $T_0$  and  $q_0$  (and consequently RH $_{\rm FT}$ ) based on an inputted  $T_{\rm SFC}$ , RH $_{\rm SFC}$ , and tropopause temperature (set to 200 K).

To facilitate comparisons with previous figures, we use the 2–12-km mean  $RH_0$  output by the model along with the prespecified  $T_{\rm SFC}$  value to interpolate model parameters onto  $T_{\rm SFC}$  versus  $RH_{\rm FT}$  parameter space shown in Figs. 3–6. It is

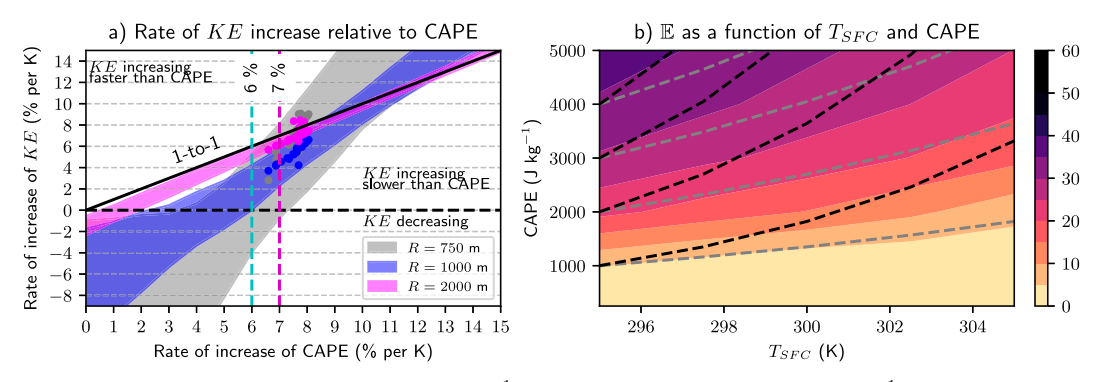


FIG. 7. (a) Rates of increase in CAPE (x axis; % K<sup>-1</sup>) vs KE of entraining parcels (y axis; % K<sup>-1</sup>), with the 1-to-1 line shown in black. Shaded regions in the y direction represent the 25th–75th percentile among profiles for a given R. Vertical cyan and magenta dashed lines denote the 6% and 7% increase in CAPE per kelvin respectively. Gray, blue, and magenta dots represent outputs from the coevolving CAPE, buoyancy, and RH experiment for 750, 1000, and 2000 m updrafts, respectively. (b) The  $\tilde{E}$  (shading; %) evaluated over the range of  $T_{\rm SFC}$  and CAPE shown on the x and y axes, respectively, with gray and black curves showing rates of increase in CAPE with  $T_{\rm SFC}$  of 6% and 12% K<sup>-1</sup>, respectively.

important to note that while RHFT and CAPE (Fig. 6a) were independent prespecified parameters in previous experiments, they are dependent model output parameters in this experiment. The only independent parameters varied among model realizations were  $T_{SFC}$  and  $\beta$  (the latter of which is shown in Fig. 6b). We first note that the analytic model only outputs a range of RHFT between roughly 40% and 80% for reasons that are discussed at length in Romps (2014), which is why large portions of the parameter space are masked as white in Fig. 6. Large values of  $\beta$  (i.e., smaller precipitation efficiencies) tend to intuitively yield larger RHFT (colors become darker toward the top of Fig. 8b) because more condensates are detrained into an updraft's surroundings and evaporated compared to when  $\beta$  is small and thus precipitation efficiency is large. CAPE no longer depends solely on  $T_{SFC}$  in this coupled tropical model, as it did in our increasing CAPE experiment. Rather, CAPE is maximized when  $\beta$  (Fig. 6b) and consequently  $RH_{FT}$  are minimized and when  $T_{SFC}$  is maximized.

Consistent with previous results,  $\tilde{E}$  generally decreases with increasing  $T_{\rm SFC}$  in both R=1000 (Fig. 8c) and R=2000 m (Fig. 8e) updrafts, evident as contours in Figs. 8c and 8e slanting toward the lower left with the smallest values toward the upper right and as greens prevalent in Figs. 8d and 8f. Consistent with the increasing CAPE experiment that was based on composites from midlatitude storm environments,  $\partial \tilde{E}/\partial z$  is somewhat consistent from -0.1% to -0.25% K<sup>-1</sup> across a wide range of parameter combinations (few contours of green shading are present in Figs. 8d,f).

Projecting  $\partial \ln \text{CAPE}/\partial T_{\text{SFC}}$  and  $\partial \ln \text{KE}/\partial T_{\text{SFC}}$  analytic model onto Fig. 7a (colored dots) allows us to understand how the rate of increase in KE relates to the rate of increase in CAPE and to understand how these relationships compare to those from our analysis of midlatitude soundings. Consistent with our analysis of Fig. 7a section 3c, rates of increase in KE generally (but not always) underpace that of CAPE (most dots fall below the 1-to-1 line). For instance, KE increases at 3%-5% K<sup>-1</sup> in 750- and 1000-m updrafts when CAPE

increases at 6.5%–7.5% K<sup>-1</sup>. As was the case in the midlatitude sounding analysis, rates of increase in KE track more closely with wider updrafts than they do with narrow updrafts (magenta dots are closer to the 1-to-1 curve than blue and gray dots). Finally, rates of increase in KE track more closely with CAPE when the rate of increase in CAPE is larger (dots fall closer to the 1-to-1 line toward the right side of the figure).

#### 4. Summary and conclusions

This article uses parcel model experiments to investigate how entrainment's influence on cumulonimbus clouds is affected by temperature, motivated by the need to understand how convective processes could respond to a warming climate. Consistent with past cloud-resolving modeling studies (Singh and O'Gorman 2015; Trapp and Hoogewind 2016), our results suggest that deep convective updrafts will generally convert a smaller fraction of their CAPE into KE in warmer climates, under plausible projected changes to relative humidity and assuming that entrainment rates do not change. Increases in CIN likely contribute to this trend, but it is clear from our results that entrainment effects should also contribute. In fact, Trapp and Hoogewind (2016) posed two hypotheses for this trend in their simulations—increasing dilution of updraft buoyancy driven by entrainment and increasing hydrometeor loading in warmer climates. Our analysis supports the first hypothesis in favor of the second, but we should emphasize that our experiment cannot holistically discount the second hypothesis.

Our parcel model experiments also reveal several nuanced insights:

- To what degree the rate of increase in KE underpaces that of CAPE depends on how quickly CAPE increases with warming.
- For rates CAPE increase of under 10% K<sup>-1</sup> (which is the most likely scenario), the rate of increase in KE should underpace that of CAPE.

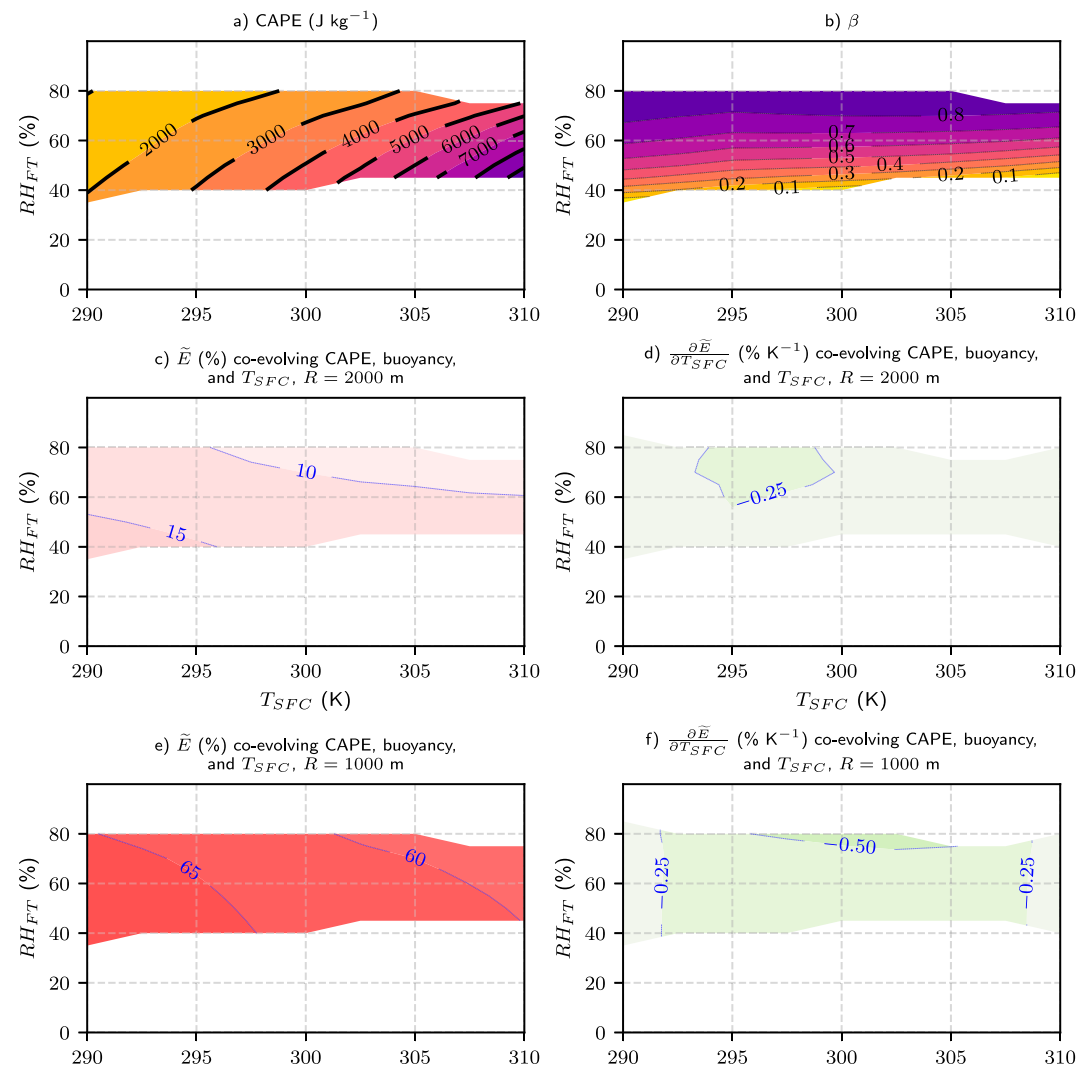


FIG. 8. (a) CAPE (J kg<sup>-1</sup>) for the co-evolving CAPE, buoyancy, and  $T_{\rm SFC}$  experiment, as a function of  $T_{\rm SFC}$  (x axis) and RH<sub>FT</sub> (y axis). (b) As in (a), but with beta shaded. (c),(d), As in Figs. 3a and 3b, but for the co-evolving CAPE, buoyancy, and  $T_{\rm SFC}$  experiment with R = 1000 m. (e),(f) As in (c) and (d), but with R = 2000 m.

- The rate of increase in KE with warming (assuming CAPE increases at less than 10% K<sup>-1</sup>) is likely to be smaller in narrow updrafts than it is in wider updrafts. Thus, climate change's effects on cumulonimbus clouds depend on their size.
- However, under circumstances where CAPE increases faster than 10% K<sup>-1</sup>, the rate of increase in KE may actually outpace that of CAPE.
- These arguments generally apply to both the tropics and midlatitudes. However, uncertainty in the rate of increase in CAPE in the midlatitudes casts a commensurate uncertainty on how quickly KE will increase.

We emphasize the need for considering entrainment in severe weather proxy studies of GCM output. Such studies often investigate trends in CAPE with warming as a gauge for storm intensity, but we have shown that increases in KE

with warming are likely to underpace increases in CAPE. This effect may be most pronounced in the context of convection initiation. For instance, initially, shallow and narrow clouds must progressively deepen and widen during the incipient stages of storm development in these environments (e.g., Peters et al. 2022a,b), and fractional entrainment rates during these early stages are often much larger than during storms' mature stages (Lasher-Trapp et al. 2021). Hence, the effect described here may contribute to an increased difficulty in convective initiation in future climates—a possibility that we plan to investigate in future work. Taken together, the above would suggest that severe thunderstorms in a warmer world would become less frequent overall but more intense when they do form. Such an outcome would be consistent with recent downscaling work (Ashley et al. 2023).

Acknowledgments. J. Peters's efforts were supported by National Science Foundation (NSF) Grants AGS-1928666 and AGS-1841674 and the Department of Energy Atmospheric System Research (DOE ASR) Grant DE-SC0000246356. D. Chavas was supported by National Science Foundation (NSF) Grants 1648681 and 2209052. Z. Lebo was supported by NSF Grant AGS-2019991. We thank Rich Thompson (NOAA SPC) for providing the T03 dataset.

*Data availability statement.* Python and MATLAB code to compute KE using an atmospheric sounding as input is available at https://doi.org/10.6084/m9.figshare.21859818.

#### APPENDIX A

#### **List of Variable Definitions**

Table A1 shows variable definitions in the main text.

TABLE A1. Variable definitions in alphabetical order. Definitions are also supplied in selected instances.

Variable symbol	Mathematical definition or value (units)	Text definition
В	$g[(T_{\rho} - T_{\rho,0})/T_{\rho,0}] \text{ (m s}^{-2})$	Buoyancy (from appendix B in Peters et al. 2022c)
$B_E \ B_{ m UD}$	$(m s^{-2})$ $(m s^{-2})$	Buoyancy of an entraining updraft parcel Buoyancy of an undiluted updraft parcel
CAPE	$\int_{z=\text{LFC}}^{z=\text{EL}_u} B_u dz \text{ (J kg}^{-1)}$	Convective available potential energy
$c_{pd} \ dh/dz$	$1005 (J kg^{-1} K^{-1})$ (unitless)	Heat capacity of dry air at constant pressure Rate of dilution of h with height
$e_0^*$	$q_0^* \frac{R_v}{R_d} p_0$ (Pa)	Saturation vapor pressure of an updraft's surroundings
ε	$\frac{2k^2L_{\rm mix}}{P_rR^2}({\rm m}^{-1})$	Fractional entrainment length scale
$ ilde{E}$	$100 \frac{\text{KE}}{\text{CAPE}}  (\%)$	Percentage of CAPE realized as KE
$egin{array}{c} \operatorname{EL}_E \ \operatorname{EL}_u \ G \end{array}$	(m) (m) 9.81 (m s <sup>-2</sup> )	Equilibrium level of an entraining parcel Equilibrium level of an undiluted parcel Gravitational constant
H	$c_{\rm pd}T + L_{v}q^* + gz \; ({ m J \; kg^{-1}})$	Moist static energy of a saturated updraft parcel
$h_0$	$c_{\rm pd}^{}T_0^{} + L_v^{}q_0^* {\rm RH}_0^{} + gz \; ({ m J \; kg}^{-1})$	Moist static energy of an updraft's surroundings
K	0.18 (unitless)	von Kármán constant
KE	$\int_{z=LFC}^{z=EL_E} B_E dz \text{ (J kg}^{-1})$	Buoyant KE of an entraining parcel at $z = EL_E$
LFC $L_m$ $L_v$ $P_r$ $q^*$ $q_0$ $q_t$ $q_v$ $R$ $R_d$ $R_{V}$ $RH_{FT}$ $RH_{SFC}$ $T$	(m) $120 \text{ (m)}$ $2501000 \text{ (J kg}^{-1}\text{)}$ $1/3 \text{ (unitless)}$ $(kg kg^{-1}\text{)}$ $(kg kg^{-1}\text{)}$ $(kg kg^{-1}\text{)}$ $(kg kg^{-1}\text{)}$ $(m)$ $287.04 \text{ (J kg}^{-1} \text{ K}^{-1}\text{)}$ $461.5 \text{ (J kg}^{-1} \text{ K}^{-1}\text{)}$ $(kg kg^{-1}\text{)}$ $(%)$ $(%)$ $(%)$ $(%)$ $(K)$ $(K)$ $T\left(1 + \frac{R_{v}}{R_{d}}q_{v} - q_{t}\right) \text{ (K)}$	Level of free convection Turbulent mixing length Reference latent heat of vaporization at the triple point temperature Turbulent Prandtl number Saturation water vapor mass fraction of an updraft parcel Saturation water vapor mass fraction of an updraft's surroundings Total vapor and condensed water mass fraction of an updraft parcel Water vapor mass fraction of an updraft parcel Updraft radius Dry specific gas constant Water vapor specific gas constant RH of an updraft's surroundings RH of the free troposphere in synthetic soundings RH at the surface in synthetic soundings Temperature of an air parcel ascending through an updraft Temperature of an updraft's surroundings Density temperature of an updraft parcel
$T_{ ho,0}$	$T_0 \left( 1 + \frac{R_v}{R_d} q_0 - q_0 \right) (\mathbf{K})$	Density temperature of an updraft's surroundings parcel
$T_{\mathrm{SF}C}$	(K)	Surface temperature in synthetic soundings
$z_{ m BL}$	Boundary layer depth in synthetic soundings (m)	
$z_{ m TR}$	Tropopause depth in synthetic soundings (m)	

#### APPENDIX B

### **Procedure for Generating Environmental Profiles**

The first step in the profile generation procedure is to determine the surface  $q_0$  using the Clausius-Clapeyron equation. Under the Rankine-Kirchhoff approximations (Romps 2021), we may integrate the Clausius-Clapeyron equation to obtain the following expressions for the saturation vapor pressures over liquid and ice, respectively (e.g., Bryan and Fritsch 2004; Romps 2017):

$$p_{sl} = p_{tr} e^{[L_v - T_{tr}(c_{pv} - c_l)/R_v](T - T_{tr}/T_{tr}T)} \left(\frac{T}{T_{tr}}\right)^{(c_{pv} - c_l)/R_v} \text{ and } (B1)$$

$$p_{si} = p_{tr} e^{[L_i - T_{tr}(c_i - c_i)/R_v](T - T_{tr}/T_{tr}T)} \left(\frac{T}{T_{tr}}\right)^{(c_l - c_i)/R_v},$$
(B2)

where variable definitions are found in Tables A1 and B1. The saturation water vapor mass fractions over liquid and ice are given by

$$q_x^* = (1 - q_t) \frac{R_d}{R_n} \frac{p_{sx}}{p_{sx} + p_0},$$
 (B3)

where x represents the condensate phase, which is either liquid (l) or solid (i). When computing lifted parcel properties, we assume that the parcel's pressure instantaneously adjusts to that of the background environment (for a detailed analysis of this assumption, see Peters and Chavas 2021). Hence, we may use Eq. (B3) with  $p_0$  for calculations of the properties of a lifted parcel later on. For a saturated parcel in the absence of condensates, Eq. (B3) may be rewritten as follows:

$$q_{x}^{*} = \frac{R_{d}}{R_{v}} \frac{e_{x}}{e_{x} \left(\frac{R_{d}}{R_{v}} - 1\right) + p_{0}}.$$
 (B4)

Hence, we obtain  $q_0$  at the surface by plugging  $T_{\rm SFC}$  and  $p_{\rm SFC}$  into Eq. (B4) and multiplying by RH<sub>SFC</sub>.

We truncate the PBL at the height of the lifted condensation level (LCL) of PBL parcels. This means that the RH in the PBL will increase from  $RH_{SFC}$  at the surface to 100% at the PBL top. Consistent with a well-mixed PBL,

we assume that  $q_0$  is constant with height in the PBL and  $T_0$  decreases with height at the unsaturated adiabatic lapse rate given by

$$\frac{dT_0}{dz} = \frac{g}{(1 - q_0)c_{\rm pd} + q_0c_{pv}},$$
 (B5)

which is integrated upward using a simple first-order upward difference scheme with a vertical grid spacing  $\Delta z=2.5$  m. These operations give us profiles of  $T_0$  and  $q_0$  in the PBL, as well as the height of the PBL top. Note that a lifted parcel and the environment will share identical temperatures and water vapor mass fractions in the PBL, and hence, the temperature T and water vapor mass fraction  $q_v$  of the parcel are simply set to  $T_0$  and  $T_0$ , respectively.

Above the PBL top, a lifted parcel will become saturated and its properties will begin to deviate from that of the background environment. We assume that the parcel is adiabatic during this period of ascent (i.e.,  $q_t$  remains unchanged) and that liquid condensate gradually freezes as its temperature cools from  $T_{\rm tr}$  to a glaciation temperature  $T_g = 253.15$  K in accordance with the following formula:

$$\omega = \frac{T - T_{\rm tr}}{T_{\rm p} - T_{\rm tr}},\tag{B6}$$

where  $0 \le \omega \le 1$  represents the ratio of frozen to liquid condensate and is set to 0 for  $T > T_{\rm tr}$  and 1 for  $T < T_g$ . We also define the saturation mass fraction of the parcel  $q^*$  such that

$$q^* = (1 - \omega)q_l^* + \omega q_i^*.$$
 (B7)

Under these conditions, an adiabatic parcel's temperature lapse rate is as follows [Eq. (25) in Peters et al. 2022c]:

$$\frac{dT}{dz} = -\frac{g}{c_{pd}} \frac{\frac{B}{c_{pm}} + 1 + \frac{L_s Q_M}{R_{m,0} T_0}}{c_{pd}} - \frac{L_i (q_t - q_{v,s}) + L_s (q_{v,s,i} - q_{v,s,l})}{c_{pd}} \frac{\partial \omega}{\partial T} + \frac{L_s L_M}{c_{pd} R_v T^2}}{(B8)}$$

where  $g=9.81~\mathrm{m~s}^{-1}$  is the gravitational acceleration,  $L_s\equiv L_{v,\mathrm{tr}}+(c_{pv}-c_l)(T-T_{\mathrm{tr}})+\omega[L_{i,\mathrm{tr}}+(c_l-c_i)(T-T_{\mathrm{tr}})],\,Q_M\equiv (1-\omega)[q_{v,s,l}/(1-\mathbb{Q}_l)]+\omega[q_{v,s,l}/(1-\mathbb{Q}_l)],\,L_M\equiv (1-\omega)L_n[q_l^*/(1-\mathbb{Q}_{v,s,l})]+\omega[q_{v,s,l}/(1-\mathbb{Q}_l)]$ 

TABLE B1. Variable Definitions specific to appendix B.

Variable symbol	Mathematical definition or value (units)	Text definition
$c_l$	4190 (J kg <sup>-1</sup> K <sup>-1</sup> )	Heat capacity of liquid water
$c_i$	$2106 (J kg^{-1} K^{-1})$	Heat capacity of ice water
$L_i$	$333000 (\mathrm{J~kg^{-1}})$	Reference latent heat of freezing valid at $T_{\rm tr}$
$p_{sl}$	Eq. (B1) (Pa)	Saturation vapor pressure over liquid
$p_{ m tr}$	Eq. (B2) (Pa)	Saturation vapor pressure over ice
$p_{\mathrm{tr}}$	611.2 (Pa)	Reference saturation vapor pressure valid at $T_{\rm tr}$
$T_{ m tr}$	273.15 (K)	Triple-point temperature
ω	Eq. (B6) (unitless)	Discriminator between liquid and ice condensate

 $\omega(L_v + L_i)[q_i^*/(1 - \mathbb{Q}_i)], \ \mathbb{Q}_x \equiv q_x^*/[(R_d/R_v) - (R_d/R_v)q_x^* + q^*],$  and B is the parcel's user-specified buoyancy. At each vertical step, all of the quantities on the right-hand side of Eq. (B5) are known, allowing us to solve for T at the next vertical level by integrating upward with a first-order upward finite-difference scheme. Concurrently, we integrate the following form of the hydrostatic equation upward using the same integration scheme to obtain  $p_0$  at the next vertical level:

$$\frac{dp_0}{dz} = -\frac{p_0 g}{R_d \left[ q_0 \left( \frac{R_v}{R_d} - 1 \right) + 1 \right] T_0}.$$
 (B9)

Once both T and  $p_0$  have been advanced to the next vertical level, the remaining unknowns at the new level are  $T_0$  and  $q_0$ . We obtain these variables using the following definition of buoyancy (derived in appendix B of Peters et al. 2022c):

$$B_u = g \frac{T_\rho - T_{\rho,0}}{T_{\rho,0}}.$$
 (B10)

Here,  $B_{\rm UD}$  is known (user specified), which leaves  $T_0$  and  $q_0$  as unknowns. Because  ${\rm RH_{FT}}$  is specified by the user, we may write  $q_0$  as a function of  ${\rm RH_{FT}}$ ,  $T_0$ , and  $p_0$  by noting that  $q_0 = {\rm RH_{FT}}q_0^*$  and using Eqs. (B7), (B6), (B2), and (B1). This leaves  $T_0$  as the only remaining unknown, which we solve using a numerical root finder in Python (fsolve in the scipi.optimize package). Above the user-specified EL height, the stratospheric temperature is held constant at its EL value, and the stratospheric  $q_0$  is set to zero.

#### APPENDIX C

### The Romps (2014) Analytic Model

The basis for the Romps (2014) analytic model for the tropical atmosphere is the "zero buoyancy assumption" popularized by Singh and O'Gorman (2013b). Under this assumption, the temperature of the tropical atmosphere tends to adjust (via compensating subsidence) to minimize the mean thermal buoyancy of deep convective updrafts. Hence, the equation for the environmental moist static energy  $h_0$  reduces to a form similar to Eq. (3):

$$\frac{\partial h_0}{\partial z} = -\frac{R_v L_v}{R_J p_0} \varepsilon (1 - RH_0) e_0^*. \tag{C1}$$

Using Eq. (C1), Romps (2014) derived the following expressions:

$$\frac{dT_0}{dz} = -\frac{R_v T_0^2}{L_v} \left( \frac{-b + \sqrt{b^2 - 4ac}}{2a} \right), \tag{C2}$$

where

$$a = \frac{R_v c_p T^2}{L_v} + q_0^*, (C3)$$

$$b = \frac{R_v c_p T_0^2}{L_v} \left( \delta - \alpha \varepsilon + \frac{g}{R_d T_0} \right) + q_0^* L_v (\delta - \varepsilon) - g, \quad (C4)$$

$$c = \left(\frac{R_v c_p T_0}{R_d L_v} - 1\right) g(\delta - \alpha \varepsilon). \tag{C5}$$

In this equation,  $dT_0/dz$  is entirely dependent on  $T_0$ ,  $q_0$ , a preprescribed  $\varepsilon$ , a preprescribed fractional detrainment rate  $\delta$ , and a preprescribed constant  $0 \le \alpha < 1$ , which is roughly equal to one minus the precipitation efficiency. Here,  $\varepsilon$  and  $\delta$  represent the mean values across a population of convective clouds. When computing ECAPE from the atmospheric profiles generated by this model, we use the separate  $\varepsilon$  values corresponding to R = 1000 and 2000 m used elsewhere in this study. This is consistent with the philosophy used in Singh and O'Gorman (2015), where we assume that while the atmosphere satisfies the zero buoyancy assumption relative to the mean  $\varepsilon$  and  $\delta$ , individual updrafts whose  $\varepsilon$  falls within the lower percentiles of the values among all clouds are capable of achieving positive buoyancy. Note that this analytic model ignores ice processes, and we therefore turn off freezing in our parcel model when applying it to the profiles resulting from the procedure described in this section for consistency. As was shown by Seeley and Romps (2016), the subjective trends output by the model should not be appreciably affected by our neglect of ice because of the coupled relationship between updraft buoyancy and environmental temperature.

Two additional equations are required to create a system that can be integrated upward to solve for  $T_0$  and  $q_0$ :

$$\frac{d \ln q_0^*}{dz} = \frac{L_v}{R_u T_0^2} \frac{d T_0}{dz} - \frac{g}{R_d T_0} \quad \text{and}$$
 (C6)

$$RH_{0} = \frac{\delta + \alpha \frac{d \ln q_{0}^{*}}{dz} - \alpha \varepsilon}{\delta + \frac{d \ln q_{0}^{*}}{dz} - \alpha \varepsilon}.$$
 (C7)

Following Romps (2014), we set  $\varepsilon = \delta$  and somewhat arbitrarily set both of these parameters to  $2.5 \times 10^{-4} \text{ m}^{-1}$ , which is a larger value than the R = 1000-m ( $1.3 \times 10^{-4} \text{ m}^{-1}$ ) and R = 2000-m ( $0.32 \times 10^{-4} \text{ m}^{-1}$ ) values used our parcel calculations, ensuring that these parcels achieve positive buoyancy.

The  $\alpha$  parameter is somewhat uncertain, so we test a range of values. It was noted in Romps (2014) that

$$\alpha < RH_0$$
. (C8)

Hence, we define a new parameter  $0 \le \beta < 1$  such that  $\alpha = \beta RH_0$  and rearrange Eq. (C7) to

$$\mathrm{RH}_0 = \frac{\delta + \frac{d \ln q_0^*}{dz} - \beta \frac{d \ln q_0^*}{dz} + \beta \varepsilon}{2\beta \varepsilon}$$

$$-\frac{1}{2}\sqrt{\left(\frac{\delta + \frac{d\ln q_0^*}{dz} - \beta \frac{d\ln q_0^*}{dz} + \beta \varepsilon}{\beta \varepsilon}\right)^2 - 4\frac{\delta}{\beta \varepsilon}}.$$
 (C9)

Our analysis varies  $\beta$  from 0 (indicating a 100% precipitation efficiency) to 0.9 (indicating a comparatively small precipitation efficiency).

#### REFERENCES

- Agard, V., and K. Emanuel, 2017: Clausius—Clapeyron scaling of peak cape in continental convective storm environments. J. Atmos. Sci., 74, 3043–3054, https://doi.org/10.1175/JAS-D-16-0352.1.
- Arakawa, A., and W. H. Schubert, 1974: Interaction of a cumulus cloud ensemble with the large-scale environment, part I. *J. Atmos. Sci.*, **31**, 674–701, https://doi.org/10.1175/1520-0469 (1974)031<0674:IOACCE>2.0.CO;2.
- Ashley, W. S., A. M. Haberlie, and V. A. Gensini, 2023: The future of supercells in the United States. *Bull. Amer. Meteor. Soc.*, 104, E1–E21, https://doi.org/10.1175/BAMS-D-22-0027.1.
- Bryan, G. H., and J. M. Fritsch, 2004: A reevaluation of ice-liquid water potential temperature. *Mon. Wea. Rev.*, **132**, 2421–2431, https://doi.org/10.1175/1520-0493(2004)132<2421:AROIWP> 2.0.CO:2.
- Chavas, D. R., and D. T. Dawson II, 2021: An idealized physical model for the severe convective storm environmental sounding. J. Atmos. Sci., 78, 653–670, https://doi.org/10.1175/JAS-D-20-0120.1
- Chen, J., A. Dai, Y. Zhang, and K. L. Rasmussen, 2020: Changes in convective available potential energy and convective inhibition under global warming. *J. Climate*, 33, 2025–2050, https://doi.org/10.1175/JCLI-D-19-0461.1.
- Christopoulos, C., and T. Schneider, 2021: Assessing biases and climate implications of the diurnal precipitation cycle in climate models. *Geophys. Res. Lett.*, 48, e2021GL093017, https:// doi.org/10.1029/2021GL093017.
- Davis, I., F. Li, and D. Chavas, 2023: Future changes in the vertical structure of severe convective storm environments over the U.S. central Great Plains. arXiv, 2310.11631v1, https://doi.org/10.48550/arXiv.2310.11631.
- Diffenbaugh, N. S., M. Scherer, and R. J. Trapp, 2013: Robust increases in severe thunderstorm environments in response to greenhouse forcing. *Proc. Natl. Acad. Sci. USA*, 110, 16361–16366, https://doi.org/10.1073/pnas.1307758110.
- Donner, L. J., T. A. O'Brien, D. Rieger, B. Vogel, and W. F. Cooke, 2016: Are atmospheric updrafts a key to unlocking climate forcing and sensitivity? *Atmos. Chem. Phys.*, 16, 12983–12992, https://doi.org/10.5194/acp-16-12983-2016.
- Douville, H., S. Qasmi, A. Ribes, and O. Bock, 2022: Global warming at near-constant tropospheric relative humidity is supported by observations. *Commun. Earth Environ.*, 3, 237, https://doi.org/10.1038/s43247-022-00561-z.
- Grabowski, W. W., and H. Morrison, 2021: Supersaturation, buoyancy, and deep convection dynamics. *Atmos. Chem. Phys.*, 21, 13 997–14 018, https://doi.org/10.5194/acp-21-13997-2021.
- Hannah, W. M., 2017: Entrainment versus dilution in tropical deep convection. J. Atmos. Sci., 74, 3725–3747, https://doi.org/ 10.1175/JAS-D-16-0169.1.
- Holloway, C. E., and J. D. Neelin, 2009: Moisture vertical structure, column water vapor, and tropical deep convection. J. Atmos. Sci., 66, 1665–1683, https://doi.org/10.1175/2008JAS 2806.1.
- Lasher-Trapp, S., E. Jo, L. R. Allen, B. N. Engelsen, and R. J. Trapp, 2021: Entrainment in a simulated supercell thunder-storm. Part I: The evolution of different entrainment mechanisms and their dilutive effects. *J. Atmos. Sci.*, 78, 2725–2740, https://doi.org/10.1175/JAS-D-20-0223.1.
- Lepore, C., R. Abernathey, N. Henderson, J. T. Allen, and M. K. Tippett, 2021: Future global convective environments in CMIP6 models. *Earth's Future*, 9, e2021EF002277, https://doi. org/10.1029/2021EF002277.

- Markowski, P., and Y. Richardson, 2010: Mesoscale Meteorology in Midlatitudes. Wiley-Blackwell, 430 pp.
- Morrison, H., 2016: Impacts of updraft size and dimensionality on the perturbation pressure and vertical velocity in cumulus convection. Part I: Simple, generalized analytic solutions. J. Atmos. Sci., 73, 1441–1454, https://doi.org/10.1175/JAS-D-15-0040.1.
- —, 2017: An analytic description of the structure and evolution of growing deep cumulus updrafts. *J. Atmos. Sci.*, **74**, 809– 834, https://doi.org/10.1175/JAS-D-16-0234.1.
- —, J. M. Peters, W. M. Hannah, A. C. Varble, and S. E. Giangrande, 2020: Thermal chains and entrainment in cumulus updrafts. Part I: Theoretical description. *J. Atmos. Sci.*, 77, 3637–3660, https://doi.org/10.1175/JAS-D-19-0243.1.
- —, and S. C. Sherwood, 2021: Comparing growth rates of simulated moist and dry convective thermals. *J. Atmos. Sci.*, 78, 797–816. https://doi.org/10.1175/JAS-D-20-0166.1.
- —, —, K. K. Chandrakar, and S. C. Sherwood, 2022: Influences of environmental relative humidity and horizontal scale of subcloud ascent on deep convective initiation. *J. Atmos. Sci.*, 79, 337–359, https://doi.org/10.1175/JAS-D-21-0056.1.
- O'Gorman, P. A., and C. J. Muller, 2010: How closely do changes in surface and column water vapor follow Clausius–Clapeyron scaling in climate change simulations? *Environ. Res. Lett.*, 5, 025207, https://doi.org/10.1088/1748-9326/5/2/025207.
- Peters, J. M., and D. R. Chavas, 2021: Evaluating the conservation of energy variables in simulations of deep moist convection. *J. Atmos. Sci.*, 78, 3229–3246, https://doi.org/10.1175/JAS-D-20-0351.1.
- —, C. J. Nowotarski, and H. Morrison, 2019: The role of vertical wind shear in modulating maximum supercell updraft velocities. *J. Atmos. Sci.*, 76, 3169–3189, https://doi.org/10.1175/JAS-D-19-0096.1.
- —, H. Morrison, W. M. Hannah, A. C. Varble, and S. E. Giangrande, 2020a: Thermal chains and entrainment in cumulus updrafts. Part II: Analysis of idealized simulations. *J. Atmos. Sci.*, 77, 3661–3681, https://doi.org/10.1175/JAS-D-19-0244.1.
- —, C. J. Nowotarski, J. P. Mulholland, and R. L. Thompson, 2020b: A formula for the maximum vertical velocity in supercell updrafts. *J. Atmos. Sci.*, 77, 3747–3757, https://doi.org/10.1175/ JAS-D-20-0103.1.
- —, C. J. Nowotarski, and G. L. Mullendore, 2020c: Are supercells resistant to entrainment because of their rotation? *J. Atmos. Sci.*, 77, 1475–1495, https://doi.org/10.1175/JAS-D-19-0316.1.
- —, H. Morrison, T. C. Nelson, J. N. Marquis, J. P. Mulholland, and C. J. Nowotarski, 2022a: The influence of shear on deep convection initiation. Part I: Theory. J. Atmos. Sci., 79, 1669–1690, https://doi.org/10.1175/JAS-D-21-0145.1.
- —, —, —, —, and —, 2022b: The influence of shear on deep convection initiation. Part II: Simulations. *J. Atmos. Sci.*, **79**, 1691–1711, https://doi.org/10.1175/JAS-D-21-0144.1.
- —, J. P. Mulholland, and D. R. Chavas, 2022c: Generalized lapse rate formulas for use in entraining CAPE calculations. J. Atmos. Sci., 79, 815–836, https://doi.org/10.1175/JAS-D-21-0118.1
- —, D. R. Chavas, C.-Y. Su, H. Morrison, and B. E. Coffer, 2023a: An analytic formula for entraining CAPE in midlatitude storm environments. *J. Atmos. Sci.*, **80**, 2165–2186, https://doi.org/10.1175/JAS-D-23-0003.1.
- ——, B. E. Coffer, M. D. Parker, C. J. Nowotarski, J. P. Mulholland, C. J. Nixon, and J. T. Allen, 2023b: Disentangling the influences of storm-relative flow and horizontal streamwise vorticity on

- low-level mesocyclones in supercells. *J. Atmos. Sci.*, **80**, 129–149, https://doi.org/10.1175/JAS-D-22-0114.1.
- —, Z. J. Lebo, D. R. Chavas, and C.-Y. Su, 2023c: Entrainment makes pollution more likely to weaken deep convective updrafts than invigorate them. *Geophys. Res. Lett.*, **50**, e2023GL103314, https://doi.org/10.1029/2023GL103314.
- Romps, D. M., 2010: A direct measure of entrainment. *J. Atmos. Sci.*, **67**, 1908–1927, https://doi.org/10.1175/2010JAS3371.1.
- —, 2014: An analytical model for tropical relative humidity. J. Climate, 27, 7432–7449, https://doi.org/10.1175/JCLI-D-14-00255.1.
- —, 2015: MSE minus CAPE is the true conserved variable for an adiabatically lifted parcel. *J. Atmos. Sci.*, **72**, 3639–3646, https://doi.org/10.1175/JAS-D-15-0054.1.
- —, 2016: Clausius–Clapeyron scaling of CAPE from analytical solutions to RCE. J. Atmos. Sci., 73, 3719–3737, https://doi. org/10.1175/JAS-D-15-0327.1.
- ——, 2017: Exact expression for the lifting condensation level. *J. Atmos. Sci.*, **74**, 3891–3900, https://doi.org/10.1175/JAS-D-17-0102.1.
- ——, 2021: The Rankine–Kirchhoff approximations for moist thermodynamics. *Quart. J. Roy. Meteor. Soc.*, **147**, 3493–3497, https://doi.org/10.1002/qj.4154.
- —, and Z. Kuang, 2010a: Do undiluted convective plumes exist in the upper tropical troposphere? *J. Atmos. Sci.*, **67**, 468– 484, https://doi.org/10.1175/2009JAS3184.1.
- —, and —, 2010b: Nature versus nurture in shallow convection. J. Atmos. Sci., 67, 1655–1666, https://doi.org/10.1175/2009JAS3307.1.
- —, and R. Oktem, 2015: Stereo photogrammetry reveals substantial drag on cloud thermals. *Geophys. Res. Lett.*, **42**, 5051–5057, https://doi.org/10.1002/2015GL064009.

- Seeley, J. T., and D. M. Romps, 2016: Tropical cloud buoyancy is the same in a world with or without ice. *Geophys. Res. Lett.*, 43, 3572–3579, https://doi.org/10.1002/2016GL068583.
- Singh, M. S., and P. A. O'Gorman, 2013a: Influence of entrainment on the thermal stratification in simulations of radiative-convective equilibrium. *Geophys. Res. Lett.*, 40, 4398–4403, https://doi.org/10.1002/grl.50796.
- —, and —, 2013b: Influence of entrainment on the thermal stratification in simulations of radiative-convective equilibrium. *Geophys. Res. Lett.*, **40**, 4398–4403, https://doi.org/10. 1002/grl.50796.
- —, and —, 2015: Increases in moist-convective updraught velocities with warming in radiative-convective equilibrium. Quart. J. Roy. Meteor. Soc., 141, 2828–2838, https://doi.org/10.1002/qj.2567.
- Thompson, R. L., R. Edwards, J. A. Hart, K. L. Elmore, and P. Markowski, 2003: Close proximity soundings within supercell environments obtained from the Rapid Update Cycle. Wea. Forecasting, 18, 1243–1261, https://doi.org/10.1175/1520-0434 (2003)018<1243:CPSWSE>2.0.CO;2.
- Trapp, R. J., and K. A. Hoogewind, 2016: The realization of extreme tornadic storm events under future anthropogenic climate change. *J. Climate*, 29, 5251–5265, https://doi.org/10.1175/JCLI-D-15-0623.1.
- Varble, A., and Coauthors, 2014: Evaluation of cloud-resolving and limited area model intercomparison simulations using TWP-ICE observations: 1. Deep convective updraft properties. J. Geophys. Res. Atmos., 119, 13891–13918, https://doi. org/10.1002/2013JD021371.
- Zhang, F., C. Snyder, and R. Rotunno, 2003: Effects of moist convection on mesoscale predictability. J. Atmos. Sci., 60, 1173–1185, https://doi.org/10.1175/1520-0469(2003)060<1173:EOMCOM> 2.0.CO:2.